Icarus **153**, 295–315 (2001)
doi:10.1006/icar.2001.6680, available online at http://www.idealibrary.com on IDEAL®

Viscous Overstability in Saturn's B Ring

I. Direct Simulations and Measurement of Transport Coefficients

Heikki Salo[1]

Department of Physical Sciences, Division of Astronomy, University of Oulu, Finland
E-mail: heikki.salo@oulu.fi

and

Jürgen Schmidt and Frank Spahn

Institute of Physics, Department of Nonlinear Dynamics, University of Potsdam, Germany

Received September 5, 2000; revised March 30, 2001

Local simulations with up to 60,000 self-gravitating dissipatively colliding particles indicate that dense unperturbed ring systems with optical depth $\tau > 1$ can exhibit spontaneous viscous oscillatory instability (overstability), with parameter values appropriate for Saturn's B ring. These axisymmetric oscillations, with scale $\sim$100 m and frequency close to the orbital period, generally coexist with inclined Julian–Toomre type wakes forming in gravitating disks. The onset of overstability depends on the internal density of particles, their elasticity, and the size distribution. The same type of oscillatory behavior is also obtained in an approximation where the particle–particle gravity is replaced by an enhanced frequency of vertical oscillations, $\Omega_z/\Omega > 1$. This has the advantage that these systems can be more easily studied analytically, as in the absence of wakes the system has a spatially uniform ground state. For $\Omega_z/\Omega = 3.6$ overstability again starts at $\tau \sim 1$. Also, nongravitating systems, $\Omega_z/\Omega = 1$, show overstability, but this requires $\tau \sim 4$. To facilitate a quantitative hydrodynamical study of overstability we have measured the transport coefficients (kinematic shear viscosity ν, kinematic bulk viscosity ζ, and kinematic heat conductivity κ) in simulations with $\Omega_z/\Omega = 3.6$, 2.0, and 1.0. Both local and nonlocal (collisional) contributions to the momentum and energy flux are taken into account, the latter being dominant in dense systems with large impact frequency. In this limit we find $\zeta/\nu \approx 2$, $\kappa/\nu \approx 4$. The dependence of pressure, viscosity, and dissipation on density and kinetic temperature changes is also estimated. Preliminary comparisons indicate that the condition for overstability is $\beta > \beta_{cr} \sim 1$, where $\beta := \partial \log(\nu)/\partial \log(\tau)$. This limit is clearly larger than the $\beta_{cr} \sim 0$ suggested by the linear stability analysis in Schmit and Tscharnuter (1995), where the system was assumed to stay isothermal even when perturbed. However, it agrees with the nonisothermal analysis in Spahn *et al.* (2000). This increased stability is in part due to the inclusion of temperature oscillations in the analysis, and in part due to bulk viscosity exceeding shear viscosity. A detailed comparison between simulations and hydrodynamical analysis is presented in a separate paper (Schmidt *et al.* 2001).

1. INTRODUCTION

One of the most puzzling features of Saturn's rings, revealed by Voyager fly-bys, is the wealth of radial structure on scales ranging from thousands of kilometers down to the resolution limit of a few kilometers (Smith *et al.* 1982, Lane *et al.* 1982). Intuitively, frequent collisions between ring particles would be expected to smooth out density gradients. This problem has inspired a great deal of theoretical efforts, concentrating mainly on the role of perturbations due to Saturn's inner satellites (begun by Goldreich and Termaine 1978, 1982). Indeed, the radial distances of the most regular density undulations in the outer A ring agree well with the locations of satellite resonances (e.g., Cuzzi *et al.* 1981, 1984, Esposito *et al.* 1983, Rosen *et al.* 1991), and both theoretical (e.g., Shu *et al.* 1985, Borderies *et al.* 1986) and numerical simulation studies (Hertzsch *et al.* 1997, Lewis and Stewart 2000) confirm that satellites are able to excite wavetrains much as observed. Similarly, resonance confinement can account for certain isolated narrow ringlets (Hänninen and Salo 1995, Goldreich *et al.* 1995). However, satellite resonances are simply too rare to explain the more irregular variations seen in the densest ring component, the B ring, lacking connection to any known resonances. It thus appears inevitable that irregular density variations must have an intrinsic origin related to some type of instability in very dense collisional systems. Recent studies (Horn and Cuzzi 1996) have also suggested that the B-ring

[1] Corresponding author: Heikki Salo. Department of Physical Sciences, Division of Astronomy, University of Oulu, PL 3000, FIN-90014 Oulun yliopisto, Finland. Fax: 358-8-553 1934.

0019-1035/01 $35.00

structure is not totally "irregular": There are signs of certain preferred length scales of the order of 20 to 100 km.

Various models for the B-ring structure have been proposed, in terms of embedded moonlets (Lissauer *et al.* 1981, Spahn and Sponholz 1989), dynamics of charged particles (Goertz and Morfill 1988), or torques exerted by micrometeoroid impacts (Durisen 1995). The originally proposed intrinsic mechanism for the generation of density variations was the *viscous instability*, based on the assumption that there is a large collision-induced difference between the kinetic temperatures of rarefied (hot) and dense (cool) portions of the rings. In this case the dynamic shear viscosity decreases with density and the collisional particle flux is directed toward local density maxima (Hämeen-Anttila 1978, Ward 1981, Lin and Bodenheimer 1981). The amplification of density variations under such conditions was also confirmed by computer simulations (Lukkari1981). However, to operate in actual rings the viscous instability requires that impacts between particles are very elastic, which is not supported by later laboratory measurements (Bridges *et al.* 1984) of the elastic properties of ice. Theoretical models (Araki and Tremaine 1986, Araki 1991) as well as computer simulations (Wisdom and Tremaine 1988) indicate stability when the measured elastic model is adopted, even in the case of an extended size distribution (Salo 1992b).

A very promising possibility now appears to be *viscous overstability* (oscillatory instability), which can take place when the dynamic shear viscosity increases with density (Borderies *et al.* 1985, Papaloizou and Lin 1988, Longaretti and Rappaport 1995, Schmit and Tscharnuter 1995). This type of density–viscosity dependence is by far more realistic, especially in extremely flattened rings. In the case of overstability the collisional flux is directed away from the local density maxima, but the system overshoots in smoothing the density gradients: Perturbations remain sinusoidal with respect to time but have exponentially growing amplitudes (in linear approximation). Superposition of such waves, with amplitudes saturated by nonlinear phenomena, might well yield structures as seen in the B ring (Schmit and Tscharnuter 1999). Such pulsational instabilities were first discussed in the context of accretion disks (Kato 1978, Blumenthal *et al.* 1984).

Most of the above cited studies of overstability have dealt with the viscous excitation of forced overstable density waves (Borderies *et al.* 1985, Papaloizou and Lin 1988, Longaretti and Rappaport 1995) using analytical approximations for the viscosity in rings with closely packed particles. However, Mosqueira (1996) carried out local simulations, where the perturbed shape of streamlines near satellite resonances was included via time-dependent radial width of the calculation region, and confirmed numerically that the theoretical conditions for overstability given in Borderies *et al.* (1985) were fulfilled in his dense B-ring model. However, due to a small number of particles (typically 40) the overstability could not be directly followed.

In our current study attention will be focused on intrinsic axisymmetric overstabilities in unperturbed rings, proposed by the hydrodynamical models of Schmit and Tscharnuter (1995; ST from hereon). In the hydrodynamical approximation the anisotropy of the velocity ellipsoid is ignored and the system is described by the density and isotropic pressure. Furthermore, all quantities are typically averaged over the vertical direction. The Navier–Stokes equations for the evolution of mean radial and tangential velocity components, combined with the continuity equation and energy equation, yield a solution for the unperturbed ground state of the system, which is characterized by a locally linear shear profile. The stability properties of this ground state can be determined by a linear stability analysis: A small perturbation of the form $\exp(ikx + \omega t)$ in density, mean velocity components, and temperature is introduced, leading to a dispersion relation for the wavenumber k of the perturbation and its complex frequency ω. The Navier–Stokes equations contain the dynamical shear and bulk viscosities, while the energy balance equation involves also a heat conduction term. Self-gravity is included via the Poisson equation, providing a link between perturbations in density and the self-gravity potential.

In the analysis of ST it is assumed that the system remains isothermal even when the density is perturbed from the ground-state value. This simplifies the treatment, by removing the energy equation, and thus the linear dispersion relation becomes a cubic equation. The evolution of perturbations is then determined mainly by the dependence of viscosity on density. ST have applied this approximation to Saturn's B ring, with the ground-state properties corresponding to typical values of the estimated B-ring temperature and density. The dependence of viscosity on density was taken from the results of previous numerical simulations (Wisdom and Tremaine 1988): It is assumed that the kinematic shear viscosity depends on optical thickness by $\nu \propto \tau^{\beta}$, with $\beta = 1.26$. According to ST the B ring should be overstable for all axisymmetric perturbations with wavelengths exceeding about $\lambda \approx 100$ m. The maximal growth rates correspond to e-folding times of the order of only a few orbital periods, for $\lambda \approx 120$ m. Also, this result is very robust to the details of the ground state: The only requirement for the onset of overstability is that the shear viscosity increases with density, with β at least slightly positive. If self-gravity is included, the minimum β is reduced even to slightly negative values.

The above-mentioned wavelength scale is easily studied by our direct particle simulations, employing a local simulation method (Salo 1992a, 1995). Interestingly, the predictions of the ST stability analysis are not consistent with numerical simulations: According to some preliminary experiments (Salo 2001), a considerably steeper viscosity vs density dependence is required than is predicted by the analysis of ST. Specifically, simulations with nongravitating particles did not show signs of overstability, although these were fairly easy to conduct for even very large optical thicknesses (up to $\tau = 3$). In principle, the reason for this discrepancy could be that the hydrodynamical treatment fails for particulate rings. However, due to the high impact frequency (several tens of impacts per orbit) the behavior of dense rings should be closely mimicked by a fluid approach (see, e.g.,

Stewart *et al.* 1984, Schmidt *et al.* 1999). Nevertheless, there are simplifying assumptions in ST's analysis, which might require reanalysis.

In Spahn *et al.* (2000) we suggested that the hydrodynamical treatment of ST should be augmented by including the energy equation in the analysis, thus accounting for the fact that the perturbed system does not instantaneously achieve isothermality but that temperatures are adjusted via the viscous gain of energy and collisional cooling and via the kinetic heat flux. The derived new fourth-order dispersion relation reproduces ST's results in the limit of infinite heat conduction but implies increased stability of dense rings for a finite heat conduction, which is at least in a qualitative agreement with the above-mentioned simulations. A further candidate for a stabilizing factor, as pointed out in Spahn *et al.* (2000), is the bulk viscosity, for which no previous estimates exist for planetary rings. More quantitative comparisons were not made in Spahn *et al.* (2000), since the new dispersion relation includes several additional parameters which are difficult to estimate analytically. For example, besides the viscosity vs density dependence utilized by ST, the dependence of dissipation, energy gain, and heat conduction on density need to be determined. Moreover, the derivatives of pressure and viscosity with respect to temperature are required. It is also important to include both local and nonlocal contributions to these quantities; the latter become very important in dense systems with a high filling factor. Thus, the new dispersion relation is most powerful in combination with detailed simulation estimates for these quantities. These estimates can be obtained from small-scale simulations ($N \sim 10^3$), whose calculation region is so small that they are not subject to overstabilities. Quantities obtained from these simulations can then be inserted into the improved dispersion relation, to yield predictions for the behavior of perturbations in larger wavelengths, studied in simulations with $N > 10^4$.

In this paper we start by showing that an overstable behavior can be seen in direct simulations, if realistically calculated self-gravity is included in dense systems (Section 2), provided that the dimensions of the calculation region are large enough to cover the most overstable wavelengths. Specifically, we demonstrate that the basically axisymmetric overstability can coexist with the nonaxisymmetric Julian–Toomre wakes which evolve in dissipative self-gravitating disks (see Salo 1992a). We further demonstrate that a qualitatively similar overstable behavior is obtained in an approximation, where the effects of the particle–particle self-gravity are mimicked solely by an enhanced vertical oscillation frequency, as in the study of dense rings by Wisdom and Tremaine (1988) (see also Lukkari and Salo, 1984). The advantage of this simple approximation is that, for systems whose dimensions fall below the regime of overstable wavelengths, it yields a steady, spatially uniform ground state. This enables the derivation of the required ground-state properties and transport quantities with respect to density and temperature (Sections 3 and 4), without the ambiguities related to the presence of nonsteady wake structures. The derived quantities will be used in the next paper (Schmidt *et al.* 2001; hereafter Paper II) for the hydrodynamical analysis of the overstability phenomenon and for the detailed comparison with the overstabilities seen in the larger scale simulations.

2. SIMULATION EXAMPLES OF OVERSTABILITY

In this section a few simulation examples of overstability will be presented, for systems with fully self-consistently calculated self-gravity. We also demonstrate that a qualitatively similar overstable behavior is achieved for a much simpler case, where the effects of self-gravity are accounted for solely by increasing the frequency of vertical oscillations with a constant factor. This latter case will also be studied in detail in the next sections, as well as in Paper II, where we compare the overstability seen in simulations with a theoretical stability analysis. For simplicity, we concentrate on the case of identical particles.

The method used in the current simulations is basically similar to that in Salo (1992a, 1995). Thus, all calculations are restricted to a local coordinate system, co-moving with the local mean angular speed of particles. Linearized dynamical equations are employed, and the particles leaving the simulation system are treated by the periodic boundary conditions, first introduced in Wisdom and Tremaine (1988) and in Toomre and Kalnajs (1991). The particle motion between impacts is governed by

$$\begin{aligned} \ddot{x} - 2\Omega\dot{y} + \left(\Omega_r^2 - 4\Omega^2\right)x &= F_x, \\ \ddot{y} + 2\Omega\dot{x} &= F_y, \\ \ddot{z} + \Omega_z^2 z &= F_z, \end{aligned} \tag{1}$$

where the x-axis points in the radial direction, the y-axis is in the direction of orbital motion, and the z-axis is perpendicular to the equatorial plane. The reference point of the coordinate system moves with angular velocity Ω in a circular orbit at a radial distance a. In the case of a central point mass, the epicyclic frequency Ω_r and the frequency Ω_z of vertical oscillations are both identical to Ω. The symbols F_x, F_y, and F_z denote additional forces (e.g., self-gravity). The boundaries are treated by assuming that each particle with a position (x, y, z) has an infinite set of image particles at $(x + nL_x, y + mL_y - 3/2nL_x\Omega t, z)$, where m and n are integers, L_x and L_y denote the dimensions of the actual calculation region, and t is the time reckoned from the beginning of the simulation. Equations (1) are invariant under this transformation. Each time a particle crosses the boundary, one of its images enters the calculation region and replaces the leaving particle. If the crossing occurs across the inner or outer boundary, the velocity of the particle is thus modified by $\Delta\dot{y} = \pm 3/2\ \Omega L_x$, which corresponds to the difference of shear velocity across L_x. In this manner the evolution of the system is independent of the choice of the origin of the coordinate system. The results are also independent of the size of the calculation region, provided that it is large compared to the mean free path between impacts (Wisdom and Tremaine 1988, Salo1991).

In the current simulations we ignore the spin of particles and assume frictionless impacts. The velocity change in impacts is

thus determined by the normal coefficient of restitution ϵ_n, describing the ratio of the post- and precollisional relative velocity components in the direction joining the particle centers. For the ϵ_n we use the standard velocity-dependent elasticity model of Bridges *et al.* (1984),

$$\epsilon_n(v_n) = (v_n/v_c)^{-0.234}, \tag{2}$$

where v_n is the normal component of the relative velocity of the impacting bodies and the scale parameter v_c equals $v_B = 0.077\ \mathrm{mm\,s^{-1}}$ in Bridges *et al.*'s (1984) measurements. This type of velocity dependence follows also from theoretical models for dissipative impacts (Spahn *et al.* 1995, Brilliantov *et al.* 1996). Two methods are used for the treatment of impacts: In the current section we use the force model introduced in Salo (1995), while the simulations in Sections 3 and 4 are carried out by following the evolution piecewise from one impact to the next, and using instantaneous velocity changes in impacts ("event-driven" method). As shown in Salo (1995) both methods yield identical results, but the former one is generally faster for self-gravitating runs. However, the event-driven method is preferred in Sections 3 and 4, as it allows easier identification of the individual impacts and the associated velocity changes, required for the evaluation of nonlocal transport quantities.

The main difference in the current self-gravitating simulations as compared to our previous simulations is the improved calculation of mutual gravitational forces. Instead of the direct particle–particle method used in Salo (1995), now only the nearby forces are calculated by a direct summation, whereas the gravitational forces from distant particles are calculated by a three-dimensional FFT method, utilizing the double periodicity of the simulated system in the planar components of a sheared coordinate system. This method, while still correctly including the effects of close gravitational encounters, enables considerably larger calculation regions and a larger number of simulation particles (by a factor of 20), which is essential for the present study. Numerical checks also indicate that the distant forces calculated with the FFT-method deviate insignificantly from those obtained with direct summation. Details of this method will be published elsewhere.

The linear stability analysis of ST predicts that the condition for overstability is that $\beta := (d\nu/d\tau)(\tau/\nu) > \beta_{cr}$, where $\beta_{cr} = \frac{1}{9}$. Thus, nongravitating simulations, which indicate a nearly linear ν vs τ dependence for $\tau \gg 1$ ($\beta \sim 1$) (e.g., Salo 1991, Section 4) should lead to overstability. For typical B-ring parameters, the predicted *e*-folding growth times are only a few orbital periods for the most overstable wavelengths of the order of 100 m. However, we have not seen any traces of such behavior in any nongravitating simulation performed up to $\tau = 3$.

The generalized linear stability analysis in Spahn *et al.* (2000) indicates that the critical β required for overstability might in fact be larger, if the effects of heat conductivity are included. Also, β_{cr} might rise close to or even above unity if the bulk viscosity significantly exceeds the kinematic viscosity. Support for this was also given by the recent two-dimensional (2-D) experiments reported in Salo (2001). Namely, in the 2-D case the impact frequency increases very strongly with τ, once the maximal packing density ($\tau_{max} = \pi/\sqrt{12} \approx 0.91$) is approached, corresponding to $\beta \approx 2$ for $\tau \approx 0.5$. In this case, the system is indeed strongly overstable, on time scales of a few tens of orbital periods. However, 2-D simulations are rather artificial, even as an approximation for a strongly flattened 3-D system. Another, more realistic way to increase β is the proper inclusion of self-gravity. For example, the vertical self-gravitational field leads to a strong enhancement of the impact frequency, both via increased frequency of vertical oscillations and via the reduced scale height, and thus, to a strong increase of viscosity with the surface density. In the case of actual particle–particle gravity the situation is more complicated than this, because of the appearance of gravitational wake structures.

In dense self-gravitating rings the particles have a tendency to form elongated trailing particle groups, dissolving and reemerging in time scales of few orbital revolutions. These are analogous to the transient wakes produced by orbital mass enhancements in a stellar disk, studied in the classical work by Julian and Toomre (1966). In particulate rings the wakes can achieve a statistical steady state as the collisional dissipation is able to balance the extra heating due to scattering by the wakes themselves. According to simulations (Salo 1992a, 1995, Daisaka and Ida 1999) the resulting velocity dispersion, measured with the Toomre Q_T parameter (Toomre 1964),

$$Q_T = \frac{c_r \Omega_r}{\pi G \sigma}, \tag{3}$$

attains a time-averaged equilibrium value of the order of 2 in the case of strong wake structure. The typical radial scale of wakes is close to Toomre's critical wavelength,

$$\lambda_{cr} = \frac{4\pi^2 G\sigma}{\Omega_r^2}, \tag{4}$$

where c_r and σ stand for radial velocity dispersion and surface density, respectively. For the Keplerian case the most unstable azimuthal wavelength is $4\lambda_{cr}$. According to the survey in Salo (1995; see also Ohtsuki and Emori (2000)) a rough criterion for the emergence of wakes is that the radial velocity dispersion maintained by impacts alone (about a few times $r\Omega$, where r is the particle radius) or by two-particle gravitational encounters (of the order of the surface escape velocity) does not exceed that corresponding to $Q_T \approx 2$.

Compared to the simulations of nongravitating particles, where typically a few hundred particles are sufficient to obtain reliable results for the collisional steady-state properties, the self-gravitating simulations require much larger particle numbers. This follows because to obtain realistic amplitudes for the wakes the size of the calculation region must exceed their scale. A rule of thumb (Salo 1995) is that the calculation region covers at least $L_x \times L_y = 4\lambda_{cr} \times 4\lambda_{cr}$ and that the gravitational forces from each particle are calculated at least up to a distance of

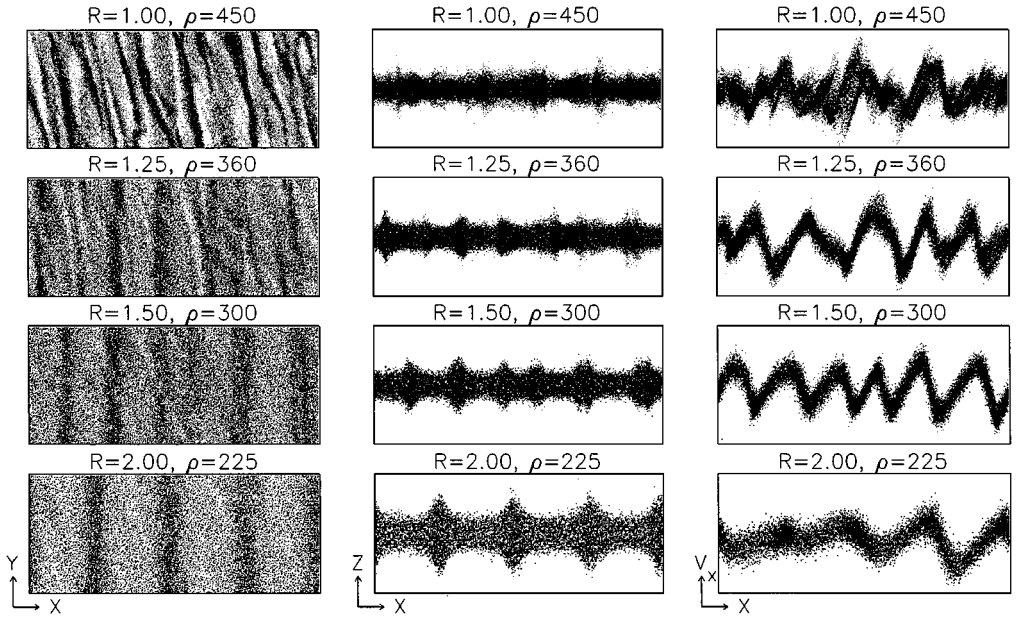

FIG. 1. Snapshots from self-gravitating simulations after evolution of 50 orbital periods. In each case a local region of 583 m × 233 m is followed, corresponding to $10\lambda_{cr} \times 4\lambda_{cr}$. The simulation parameters are $\tau = 1.4$, $\sigma = 840$ kg m^{-2}, and the Saturnocentric distance is 100,000 km ($\Omega = 1.945 \times 10^{-4}$ s^{-1}). The four different examples correspond to different combinations of particles' internal density ρ and radius r: To maintain fixed σ and τ the product $r\rho$ is kept fixed. The number of particles is between 15,000 and 60,000. In the leftmost column the system is shown from above (the planet is to the left, and the direction of the mean orbital motion is up), while in the middle column the system is shown from the side (the vertical extent of the frame is $\pm 0.25\lambda_{cr}$). In the right column the radial velocity profile is shown (vertical range is ± 0.8 cm s^{-1}, corresponding to $20\,r\Omega$ for 1-m particles). The elasticity of impacts is described by the Bridges *et al.* (1984) formula. The self-gravity is calculated with FFT, using an $n_x \times n_y \times n_z = 256 \times 64 \times 8$ density grid, combined with a pairwise calculation of particle–particle forces for mutual distances smaller than $\lambda_{cr}/5$. In each of the runs the Toomre parameter is $Q_T \sim 1$, before the onset of overstability.

$2\lambda_{cr}$. For simulations describing Saturn's B ring these conditions imply that at least about 10^4 particles are needed, even when limiting the simulation to identical particles. To search for possible overstable behavior even larger regions are required, especially in the radial direction.

In principle, the presence of wakes makes the distinction of overstable behavior in simulations somewhat difficult, especially because the radial scale of the wakes falls to about the same parameter region as that expected for overstability, and also because of the rapid growth rates and the saturation of wakes to large amplitudes. Nevertheless, with suitable parameter values both wakes and overstabilities can be seen simultaneously. Such a demonstration is provided by Fig. 1, for an optically thick ($\tau = 1.4$) ring. Four different simulations are shown, differing in the internal density of particles ($\rho = 225{-}450$ kg m^{-3}), while the surface density is kept constant ($\sigma = 840$ kg m^{-2}). The size of the simulation region covers $L_x \times L_y = 10\lambda_{cr} \times 4\lambda_{cr}$, with $\lambda_{cr} = 58.3$ m.

For the case with $\rho = 450$ kg m^{-3} the behavior is dominated by nonaxisymmetric transient wakes, inclined by about 20° with respect to the tangential direction, in accordance with previous studies. Also, the most prominent radial wavelength of these inclined structures is close to λ_{cr}. However, due to low internal density of particles the Toomre parameter is only about $Q_T \sim 1$, in contrast to $Q_T \sim 2$ found in earlier simulations performed mainly for solid ice density. As the internal density further decreases, the wake structure weakens, basically because the maximal mass density the wakes can attain is reduced. Simultaneously, a new type of oscillating, axially symmetric structure becomes visible in wavelengths of 100–150 m. The *e*-folding times of the amplitude of these structures is of the order of few tens of orbital periods. In the case $\rho = 360$ kg m^{-3}, both axisymmetric and nonaxisymmetric structure is seen simultaneously. Fourier analysis reveals the presence of weak axisymmetric waves also in the wake-dominated case $\rho = 450$ kg m^{-3}, as well as the presence of weak nonaxisymmetric wakes even in the $\rho = 225$ kg m^{-3} case. The axisymmetric oscillations are also visible in the velocity profiles.

A demonstration that we are indeed dealing with an overstability is provided by Fig. 2, where the evolution of perturbations is followed for one orbital period for the simulation with $\rho = 300$ kg m^{-3}. Different time steps are represented by different curves in the same frame. All studied quantities show oscillations with a period close to one orbital revolution, with phase shifts between density and radial and tangential velocities in accordance with theoretical expectations for overstability (Paper II). Figure 2 also shows two simpler cases, where the overstability is retained. In Fig. 2b only the vertical component of self-gravity is included, whereas the planar components of self-gravity are set to zero, and in Fig. 2c the self-gravity is approximated by the aforementioned increase of vertical frequency. Here we have taken $\Omega_z/\Omega = 3.6$, the same value studied

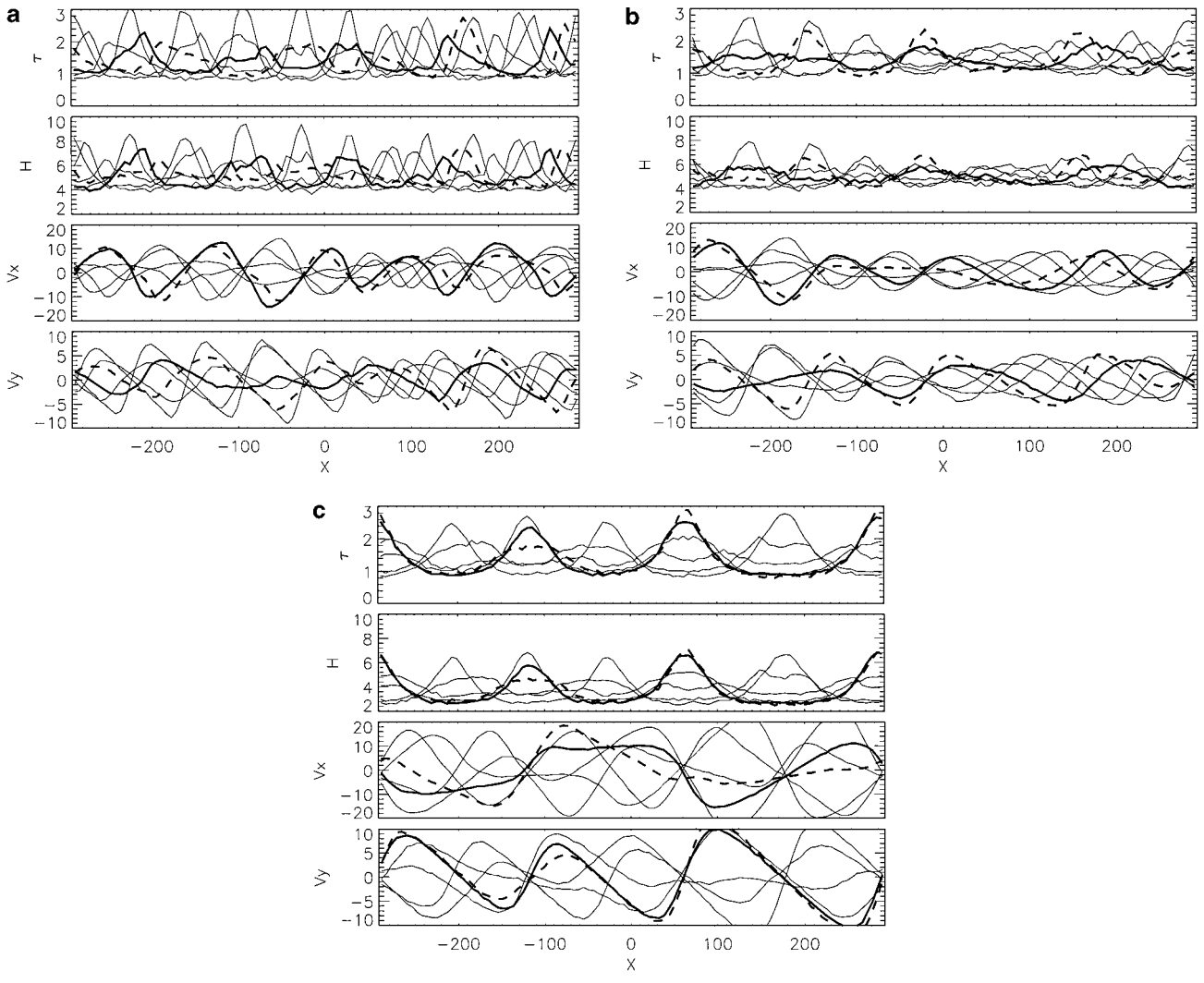

FIG. 2. The evolution of radial perturbation profiles over one orbital period (after evolution of 100 periods). The thick solid and dashed lines correspond to the beginning and the end of the interval, respectively. Three different cases are compared: In (a) the run corresponds to the self-gravitating $\rho = 300$ kg m^{-3} example of Fig. 1, (b) is similar except that only the vertical component of self-gravity is included, while the planar components are set to zero, and in (c) the particle–particle self-gravity is altogether ignored but the frequency of vertical oscillations is increased by a factor of 3.6. Perturbations in optical depth τ, local vertical thickness $H = \sqrt{6\langle z^2\rangle}$, radial velocity v_x, and shear corrected tangential velocity $v_y + 1.5\,\Omega x$ are shown (velocity unit is $r\Omega$, while the unit of H is r).

by Wisdom and Tremaine (1988) and in Salo (1991). Except for the different dominant wavelength and different amplitude of perturbations, the qualitative behavior in all three cases is very similar. This suggests that the overstability is not tied to the inclusion of self-gravity itself but rather to the modified viscous properties of the system.

A qualitative difference between true self-gravitating systems and those with an enhanced vertical frequency (or with just the vertical component of self-gravity) is however seen in the frequency of overstable oscillations (Fig. 3). For the approximative cases the frequency of overstable oscillations always exceeds the orbital frequency, with the difference increasing toward smaller wavelengths. In the case of actual particle–particle gravity the oscillation period is generally longer than the orbital period, although the frequency turns again into a rise at smaller wavelengths. As will be shown in Paper II, the increased frequency as compared to orbital frequency is just what is expected from pressure and viscosity effects, while the reduced frequency reflects the slowdown of epicyclic oscillations due to self-gravity (e.g., Toomre 1964).

Figure 4 shows another comparison of the above runs, displaying the evolution of the dispersion of the radial velocities, $\sqrt{\langle v_x^2\rangle}$, calculated for the whole simulation system. The behavior of this quantity provides a good indication of overstable behavior. In the absence of systematic oscillations $\sqrt{\langle v_x^2\rangle}$ will equal the local velocity dispersion, thus attaining a steady-state value after a few tens of impacts/particle. In the case of overstability $\sqrt{\langle v_x^2\rangle}$ becomes more and more dominated by the total squared amplitude of systematic oscillations, $\langle v_x^2\rangle = \sum_k A_k^2$, where A_k denote the velocity amplitudes of different axisymmetric modes allowed

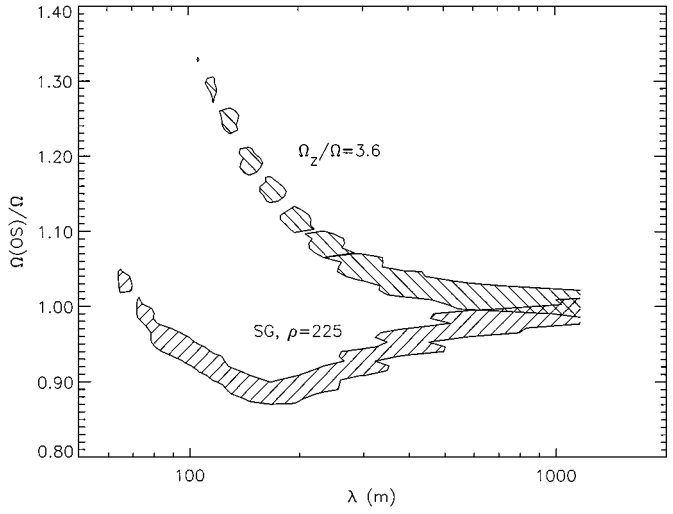

FIG. 3. The frequency of axisymmetric oscillations as a function of wavelength, in the case of particle–particle gravity ($\tau = 1.4$, $\rho = 225$ kg m^{-3}) and in the case of an enhanced vertical frequency ($\Omega/\Omega_z = 3.6$). The runs correspond to those in Fig. 1, except that radial length is $20\lambda_{cr} = 1166$ m. The frequencies are calculated with the Lomb normalized periodogram (see Press *et al.* 1992, p. 569), using radial velocities from the first 20 orbital periods of evolution.

by the calculation region (θ_k stands for the phase of the mode):

$$v_x(x) = \sum_k A_k \cos\left[k\left(\frac{2\pi x}{L_x} - \theta_k\right)\right], \quad k \geq 1. \qquad (5)$$

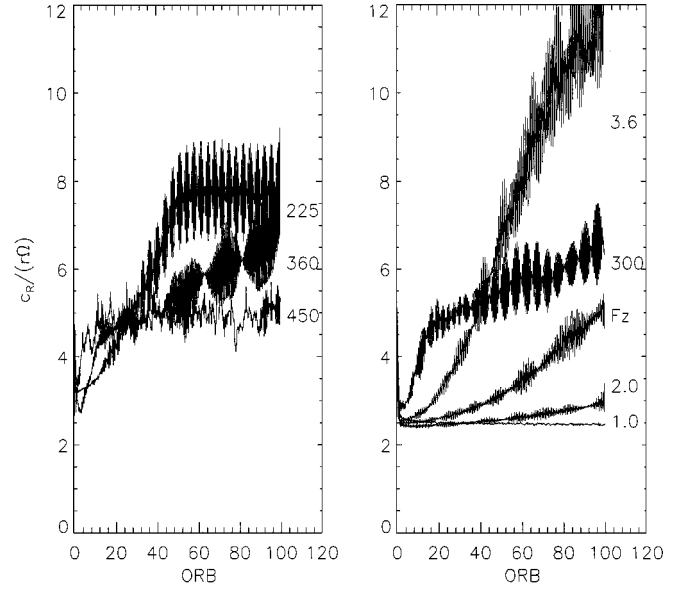

FIG. 4. Evolution of the total rms radial velocity in simulations. In the left three self-gravitating runs of Fig. 1 with different ρ's are compared, while in the right several types of simulations corresponding to $\rho = 300$ kg m^{-3} are shown, The curve labeled "Fz" corresponds to only vertical gravity, while the runs labeled "3.6" and "2.0" correspond to nongravitating runs with enhanced vertical frequency. The curve "1.0" stands for a nongravitating simulation ($\Omega = \Omega_z$).

In the case with only weak overstability ($\rho = 450$ kg m^{-3}) the rms velocity dispersion is mainly determined by the wakes, whose transient nature leads to irregular fluctuations in $\sqrt{\langle v_x^2 \rangle}$. The other two curves in Fig. 4a indicate the signature of growing overstable amplitudes. Also shown in Fig. 4b are comparisons between the realistic particle–particle self-gravity and the two above-mentioned approximations. It can be seen how increasing the ratio Ω_z/Ω leads to a more rapid growth of overstabilities. Also shown is a nongravitating simulation where $\Omega_z = \Omega$, showing the establishment of a steady state with no signs of overstable fluctuations.

During the simulations there is a tendency for the prominent axisymmetric wavelength to increase. For example, in the run with $\rho = 225$ kg m^{-3}, the dominant radial wavenumber $k = 4$ seen in Fig. 1 is gradually displaced by $k = 3$, as the run was continued to 200 orbital periods. Note that, due to the periodicity of the simulation region, only wavelengths which are integer fractions of its radial extent can grow. It is thus important to check that the size of the calculation region is large enough so that the periodic boundaries do not affect the growth of dominant overstable modes. For this purpose an additional simulation was performed, corresponding to the $\rho = 225$ kg m^{-3} case shown in Fig. 1, except for twice the number of particles and with a twice larger radial extent (same run as studied in Fig. 3). This run retained the growth on the same absolute radial scales (now $k = 7$ was dominant after 200 orbital periods), and with similar *e*-folding times. This confirms that the periodic boundary conditions are not responsible for the obtained overstabilities, nor do they affect the observed behavior, at least not in scales which are a few times smaller than the calculation region. Also, in all the above simulations a small initial seed was given for the axisymmetric velocity perturbations, amounting to 2×10^{-4} m s^{-1} for each A_k with $k = 1$–30. A comparison simulation without such a seed (amplitudes of initial noise are about 10 times smaller than the amplitude of seed) yielded practically identical behavior, except for a time delay of about 20 orbital periods before the overstability became visible. Similarly, the onset of overstability is delayed if the tangential size of the calculation region is increased, leading however to identical evolution.

A brief survey of self-gravitating simulations similar to the $\rho = 225$ kg m^{-3} case in Fig. 1 indicated that overstability starts when $\tau \approx 1.2$ (Fig. 5). For larger ρ's the strong wake structure appears to limit the growth of overstable modes. Nevertheless, for $\rho = 450$ kg m^{-3} the system is clearly on the verge of overstability: A small reduction in the amplitude of the wakes, induced by cutting the region from which the gravity is calculated (see Salo 1995), is sufficient to allow the growth of prominent axisymmetric oscillations similar to those seen for smaller ρ'*s*. For example, by limiting gravity to that exerted from the region within one λ_{cr} around each particle, signs of overstability are visible already for $\tau = 1$. The onset of overstability is also sensitive to the elasticity assigned to the impacts as well as to the particle size distribution. For example, the overstability was still obtained (for $\tau = 1.4$, $\rho = 225$ kg m^{-3})

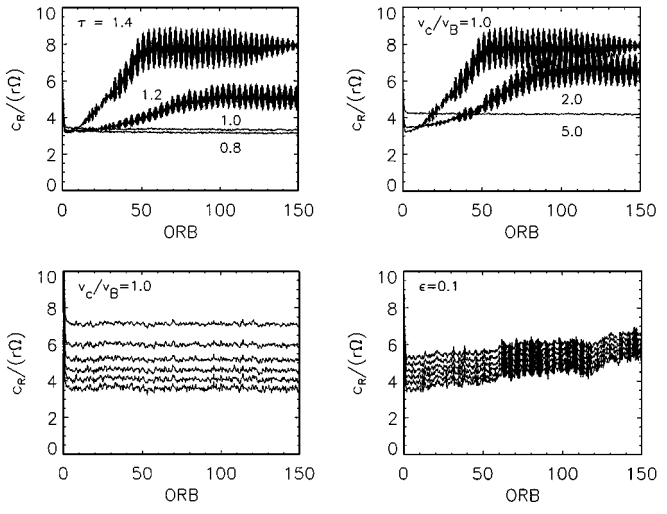

FIG. 5. The onset of overstability in simulations with different τ, ϵ_n, and size distribution, measured in terms of the total rms radial velocity. In the upper left frame four different values of τ are compared, while in the upper right the velocity scale parameter in Bridges *et al.*'s formula is varied. The two lower frames display two runs with a power-law size distribution ($r_{min} = 0.5$, $r_{max} = 5$ m, exponent $q = 3$), with two different elasticity models: The evolution of velocity dispersion is shown separately for six logarithmic size bins (smaller particles have larger dispersion). In all cases the internal density of particles is $\rho = 225$ kg m^{-3}.

when the velocity scale parameter v_c in Bridges *et al.*'s formula (Eq. 2) was doubled, whereas with $v_c/v_B = 5$ the system became stable (increased v_c/v_B implies increased steady-state velocity dispersion). Also, when using a power-law size distribution, $n(r) \sim r^{-q}$, with $r_{min} = 0.5$, $r_{max} = 5$ m, and $q = 3$, yielding the same τ and σ, the system remained stable for Bridges *et al.*'s formula. This increased stability is likely to be related to the increased velocity dispersion achieved by small particles. However, with increased dissipation and constant $\epsilon_n = 0.1$, overstability was again achieved even with size distribution. These few examples already indicate that the onset of overstability in dense rings is very dependent on the various, still poorly constrained parameter values.

A more detailed analysis of the overstable behavior in simulations, utilizing the transport coefficients derived in the next two sections for systems with enhanced vertical oscillation frequency, is left to Paper II. The main emphasis will be on the case $\Omega_z/\Omega = 3.6$. This value is chosen, partly because it enables the comparison to some previous simulations (e.g., those by Wisdom and Tremaine 1988) and also because it leads to a rapid growth of overstabilities, so that they are more easily followed to the nonlinear regime.

3. EVALUATION OF QUANTITIES NEEDED IN HYDRODYNAMICAL ANALYSIS

In this and the next section we will study the approximation where the particle–particle self-gravity is replaced by an enhanced vertical frequency. As shown above this simplification can also lead to overstable behavior, retaining the same qualitative characteristics as the more realistic self-gravitating case. The main advantage is that for systems whose dimensions are below the regime of overstable behavior, the evolution now leads to a uniform stationary steady state, as required when applying linear stability analysis.

In the analysis of ST the ground state was described by the surface density σ and by the distance from the planet, through Ω. The isotropic kinetic pressure p was identified with σT, where $T = c_0^2$ is the kinetic temperature (c_0 is the 1-dim velocity dispersion) and the kinematic viscosity ν was assumed to be of the form $\nu = \nu_0(\sigma/\sigma_0)^\beta$. Values for σ_0, Ω, c_0, and ν_0 where chosen to represent the dense parts of Saturn's B ring. In the nonisothermal stability analysis of Spahn *et al.* (2000), which takes into account the energy equation, several additional quantities are required. For example, we will need the cooling function Γ, giving the dissipative loss of energy, and the heat conductivity κ, connecting the kinetic heat flux to the temperature gradient. In addition we need to know the derivatives of p, ν, and Γ with respect to T for a fixed density. Besides shear viscosity, related to the flow of momentum in the presence of velocity shear, we also need the bulk (expansion) viscosity ζ, related to the irreversible flow of energy into internal degrees of freedom due to compression. For all components of the pressure tensor we will consider both local and nonlocal contributions; the latter arises because the particle locations in impacts correspond to slightly different mean radial distances (Araki and Tremaine 1986, Shukman 1984). In dense systems the latter contribution to pressure and viscosity is often dominant.

3.1. Equations for Transport Quantities

Let us denote the particle positions by $x_i = \{x, y, z\}$ and their velocities by $v_i = \{\dot{x}, \dot{y}, \dot{z}\}$. Further, denote the mean velocity $\mathbf{u} = \langle \mathbf{v} \rangle$ so that a particle's random velocity is $\mathbf{c} = \mathbf{v} - \mathbf{u}$. The kinetic temperature is defined as $T = \frac{1}{3}\,\mathrm{tr}\langle c_i c_j \rangle$. In a spatially uniform steady state there is a linear shear profile $\mathbf{u} = \{0, -3/2\Omega x, 0\}$. However, we will also study cases where there is an additional perturbation $\delta\mathbf{u} = \{\delta u_x, \delta u_y, 0\}$ depending on the x-coordinate.

The flow of momentum consists of the local contribution, related to the momentum carried by particles' random motions, and the nonlocal contribution, resulting from momentum transfer from one particle to another during a collision. The former can be expressed as (averaging over vertical direction is assumed in what follows)

$$P_{ij}^{local} = \sigma \langle c_i c_j \rangle, \tag{6}$$

while the nonlocal contribution is

$$P_{ij}^{nonlocal} = \frac{\sigma \sum \Delta x_i \delta c_j}{N \delta t}. \tag{7}$$

Here the sum is over all impacts taking place during the time interval δt, while Δx_i is the absolute difference of the i-coordinates

of the impacting particles, and δc_j is the change in the j-coordinate of the velocity of the particle with larger x_i. The number of particles is denoted by N. The same formulations have been used by Wisdom and Tremaine (1988) and by Mosqueira (1996).

In the hydrodynamical description the pressure tensor is written as

$$\hat{P} = p\hat{U} - 2\eta\hat{D} - \xi\hat{U}\boldsymbol{\nabla}\cdot\mathbf{u}, \tag{8}$$

where p is the isotropic pressure, η and ξ stand for the dynamic shear and bulk viscosities ($\eta = \sigma\nu$, $\xi = \sigma\zeta$), respectively, $\hat{U}$ is the unit tensor, and $\hat{D}$ the shear tensor

$$D_{ij} = \frac{1}{2}\left(\nabla_i u_j + \nabla_j u_i - \frac{2}{3}\delta_{ij}\nabla_k u_k\right). \tag{9}$$

Since $\mathrm{tr}\,\hat{D} = 0$ and in the steady state we have $\boldsymbol{\nabla}\cdot\mathbf{u} = 0$, it follows that

$$p = \frac{1}{3}\,\mathrm{tr}\,\hat{P} = \frac{1}{3}\,\mathrm{tr}(\hat{P}^{local} + \hat{P}^{nonlocal}) \equiv p^{local} + p^{nonlocal}. \tag{10}$$

We will determine both pressure components separately. Similarly, for the nondiagonal component we have $D_{12} = -\frac{3}{4}\Omega + \frac{1}{2}\partial_x\delta u_y + \frac{1}{2}\partial_y\delta u_x$, affording an equation from which shear viscosity can be derived. Specifically, if there are no systematic motions ($\delta u_x = 0$, $\delta u_y = 0$) this yields

$$\eta = \frac{2}{3\Omega}P_{12} \equiv \eta^{local} + \eta^{nonlocal}, \tag{11}$$

with similar identification of local and nonlocal components as for the pressure.

Equation (8) also provides means for the estimation of bulk viscosity. Assume that the system is perturbed so that the compression $\boldsymbol{\nabla}\cdot\mathbf{u}$ is nonzero. Further, assume that various quantities are separately collected for different radial zones of the system. Due to compression the instantaneous isotropic pressure $p(t)$ in each zone will then deviate from $p_c(\sigma(x,t))$, which is the steady-state pressure corresponding to the instantaneous density σ. Taking the trace of Eq. (8) affords

$$p - p_c = -\xi\boldsymbol{\nabla}\cdot\mathbf{u}, \tag{12}$$

providing a relation from which ξ can be obtained. Again, the division to local and nonlocal components will be made.

The kinetic heat flux $\mathbf{q}$ is related to the transport of random kinetic energy, $E = c^2/2$ (here we use energy/particle mass), which also takes place both via particles' motion and during impacts. For the local flux we have

$$q_i^{local} = \sigma\langle Ec_i\rangle = \frac{1}{2}\sigma\langle c^2 c_i\rangle. \tag{13}$$

The treatment of nonlocal energy flux is somewhat more problematic, as we must separate the dissipational loss of kinetic energy from the transfer in the impacts. This is achieved by splitting the velocities $\mathbf{v}_k$ of impacting particles (with $k = 1, 2$) into the center of mass velocity $\mathbf{v}_c = 0.5\,(\mathbf{v}_1 + \mathbf{v}_2)$ and the relative velocity $\mathbf{g} = \mathbf{v}_2 - \mathbf{v}_1$. With these definitions we obtain for the velocities and the related kinetic energies of the particles (with $+$ and $-$ signs corresponding to particles $k = 2$ and 1, respectively)

$$\mathbf{v}_k = \mathbf{v}_c \pm \frac{1}{2}\mathbf{g}, \tag{14}$$

$$E_k = \frac{1}{2}\mathbf{v}_k^2 = \frac{1}{2}\left\{\mathbf{v}_c^2 + \frac{1}{4}\mathbf{g}^2 \pm \mathbf{v}_c\cdot\mathbf{g}\right\}. \tag{15}$$

Taking into account that only the relative velocity is altered due to the collision according to

$$\mathbf{g}' = \mathbf{g} - (1+\epsilon)\,(\mathbf{g}\cdot\mathbf{n})\,\mathbf{n}, \tag{16}$$

where the prime labels the value after the collision and $\mathbf{n}$ is the unit vector pointing from particle 1 to 2, we obtain the change of the kinetic energy for the particle k:

$$\delta E_k = E_k' - E_k = \frac{\epsilon^2 - 1}{8}(\mathbf{g}\cdot\mathbf{n})^2 \pm \frac{1+\epsilon}{2}(\mathbf{g}\cdot\mathbf{n})(\mathbf{v}_c\cdot\mathbf{n}). \tag{17}$$

The first term is the energy dissipation in the impact; the second is the transported energy. To separate the transport part we define

$$E_k^s = E_k - \frac{1}{2}(E_1 + E_2), \quad k = 1, 2, \tag{18}$$

where E_1 and E_2 are kinetic energies of the particles participating in the impact. Now we define $\delta E_k^s = E_k'^s - E_k^s$, which equals, except for the sign, the last term in Eq. (17). The nonlocal energy flux can then be written as

$$q_i{}^{nonlocal} = \frac{\sigma\sum\Delta x_i\delta E^s}{N\delta t}, \tag{19}$$

where Δx_i is as before and δE^s is the change associated with the particle with the larger x_i-coordinate. Note that the last term in Eq. (17) is related to the "dynamical friction" term in Ohtsuki (1999), which in the case of unequal-sized particles works toward energy equipartitioning between different size populations.

In the hydrodynamical treatment the heat flux is assumed to depend linearly on the temperature gradient,

$$\mathbf{q} = -\kappa_D\boldsymbol{\nabla}T, \tag{20}$$

where κ_D is the dynamic heat conductivity. Again, identifying this with Eqs. (13) and (19) offers means for evaluating both the local and nonlocal heat conductivity.

3.2. Practical Evaluation of Transport Quantities

The most important advantage of the local method is that the optical thickness of the system is controlled by the number of particles and the size of the calculation region. It is thus possible to determine the density dependence of all quantities of interest by conducting a series of separate experiments for different densities. The above formulas for $X = \{p, \Gamma, q, \eta, \xi, \kappa_D\}$ use dynamic quantities containing the surface mass density, whereas the current simulations operate with massless particles. To facilitate the application of hydrodynamic equations we will systematically replace σ by optical thickness τ and define the corresponding simulation quantities by

$$X_{sim} \equiv K X, \tag{21}$$

where $K = \tau/\sigma$ is the mass extinction coefficient. Thus, for example,[2] $p^{local}_{sim} \equiv \tau T$. Also, what we actually measure from simulations are the kinematic transport quantities $\nu = \eta/\sigma$, $\zeta = \xi/\sigma$, and $\kappa = \kappa_D/\sigma$.

3.2.1. Shear Viscosity

The evaluation of the shear viscosity is based on Eq. (11) and is carried out in a straightforward manner, as in Wisdom and Tremaine (1988) and Salo (1991). A good accuracy can be achieved, as ν can be measured in a uniform steady state, and thus averages can be taken over all particles in the system and over arbitrarily long periods of time once the steady state is achieved. The same runs are also used for the evaluation of steady-state values of T, p, and Γ_{sim} as functions of τ.

The values of the viscosities obtained can be checked by observing that the values of implied viscous gain balance the collisional dissipation of energy, measured directly by summing the individual energy losses in impacts. In the steady state we must have $\Gamma_{sim} = \frac{9}{4}\Omega^2\tau\nu$. As shown in Fig. 6 this balance is satisfied to great accuracy, for both small and large τ. Since different contributions to the viscosity are dominant in these two limits, this confirms the correctness of both the local and nonlocal viscosities.

3.2.2. Bulk Viscosity

Compared to the evaluation of shear viscosity, the basic difficulty is that bulk viscosity can only be measured in a presence of compression. In practice we proceed as follows: An initial radial velocity gradient is introduced in the x-direction by adding a sinusoidal velocity increment,

$$\delta v_x(x) = A_v \cos(2\pi x/L_x), \tag{22}$$

[2] We drop the subscript "sim" from pressure, to avoid using simultaneous sub- and superscripts, but we retain its use for Γ and q.

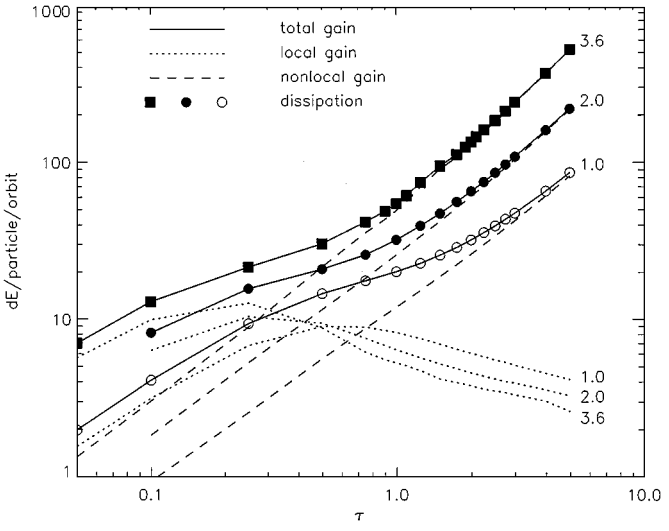

FIG. 6. Check of the shear viscosity measurements. Solid line indicates the total viscous gain of energy, $G_{sim} = \frac{9}{4}\Omega^2\nu\tau$, while dotted and dashed lines show separately the local and nonlocal contributions, respectively. The symbols indicate the directly measured energy dissipation Γ_{sim} in impacts. The overlap of G_{sim} and Γ_{sim} indicates that the energy balance $G_{sim} - \Gamma_{sim} = 0$ is very accurately satisfied. The energies are normalized by $(r\Omega)^2$ and they correspond to the change of energy/particle/orbital period.

to each particle. This causes a standing radial compression wave with a decaying amplitude. The instantaneous pressures p^{local} and $p^{nonlocal}$ and the values of τ are then tabulated for short time intervals (typically 20 intervals per orbital period) for different radial zones of the system (typically for 20 zones). Similarly, the mean radial velocities are collected for these time intervals and zones, to obtain $\Delta = \nabla \cdot \mathbf{u} = \partial \delta u_x/\partial x$ (since there is compression only in the x-direction; the system also develops systematic y-motions, due to the added δu_x-perturbation, but these are much weaker, and most importantly depend only on x, not on y).

The steady-state values of pressure, $p_c(x, t)$ corresponding to instantaneous $\tau(x, t)$, are calculated with the help of the $p^{local}(\tau)$ and $p^{nonlocal}(\tau)$ relations, constructed in the separate runs utilized in the evaluation of shear viscosity. In practice, a second-degree interpolation between the tabulated discrete density values is sufficient. With the above procedure we have for each time interval and radial zone certain values of Δ and pressure deviations $p - p_c$. A least-mean-square fit is made to all of these values. The initial evolution, when the system's temperature is still evolving toward equilibrium, is eliminated: This relaxation period can be made very short by carefully choosing initial values close to equilibrium. Also, to have better statistics, the velocity perturbation can be repeated several times; this is important in cases where the compression wave is rapidly decaying.

To check this method we must be sure that the relation between Δ and $p - p_c$ is indeed linear and that the proportionality factor is independent of the applied velocity perturbation, as long as this is small. For systems with potentially overstable behavior

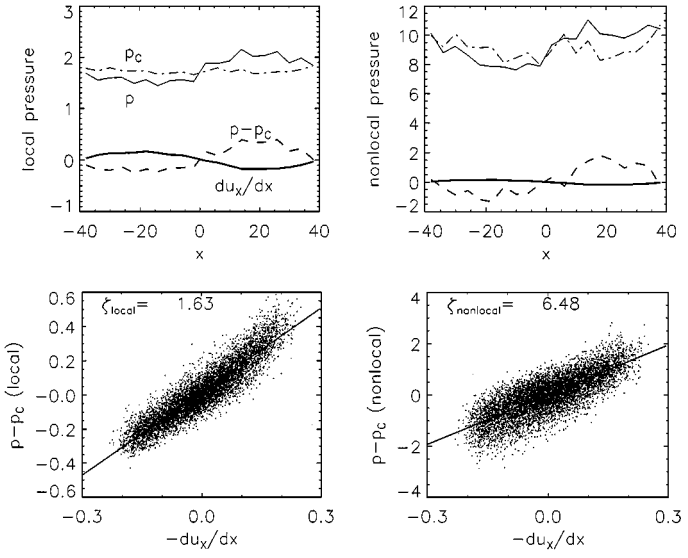

FIG. 7. Example of the determination of bulk viscosity, for $\tau = 0.5$ and $\Omega_z/\Omega = 3.6$. In the upper frames the solid line and the dash-dotted line denote the instantaneous pressure p and the equilibrium pressure p_c corresponding to the instantaneous density, respectively. The dashed line denotes $p - p_c$, while the thick solid line is the instantaneous compression. One single collection interval of 0.05 orbital periods is shown. In the lower frames, all data points (20 zones and 400 collection intervals) from the same run are displayed simultaneously, together with a linear fit whose slope gives the bulk viscosity coefficient. Simulation quantities are used (see Section 4) and the units of pressure and the kinematic bulk viscosity are $(r\Omega)^2$ and $r^2\Omega$, respectively. The amplitude of initial radial velocity perturbations amounted to $2r\Omega$.

care must be taken so that the dimensions of the calculation region are small enough or that the measurement is short enough because otherwise the amplitude of oscillations might grow to excessively large values. The upper row of Fig. 7 displays an example of how the pressure deviations relate to compression for a single instant of time. When collected over the whole run (lower row), the overall linear trend is evident, although there is considerable noise present. In the example shown the amplitude of velocity perturbation amounted to $A_v = 2r\Omega$. This is a fairly large perturbation (comparable to the radial velocity dispersion), causing about a 20% oscillation of the optical depth. Nevertheless, the mean T in this run is only about 2% larger than in the absence of extra velocity perturbation. A corresponding run with $A_v = r\Omega$ yields similar values for both ζ^{local} and $\zeta^{nonlocal}$, within about 3% accuracy. If the amplitude is further decreased the results become excessively affected by noise. In all the subsequent measurements $A_v = 2r\Omega$ was used.

3.2.3. Heat Conductivity

As in the measurements of bulk viscosity, the heat conductivity could in principle be evaluated by introducing an initial, decaying temperature perturbation to the system. However, there is an alternative way, enabling a more accurate determination. Namely, we can create a steady, nonuniform temperature profile, by making the elasticity of impacts depend slightly on the position. Since we are interested in the radial heat conduction this is done by

$$v_c(x) = v_B[1 + A_\epsilon \cos(2\pi x/L_x)], \tag{23}$$

where v_c is the velocity scale parameter used in the Bridges-type elasticity law and v_B is the original parameter for Bridges *et al.*'s formula. Similarly, if we are interested in a system with a constant coefficient of restitution, a small sinusoidal variation with x is introduced to the desired mean value of ϵ_n.

As long as A_ϵ is small, this produces an almost sinusoidal radial variation in the equilibrium T which is continuous over the radial boundaries. The advantage is that once the (nonuniform) steady state has been established, all quantities necessary for the evaluation of κ can be time-averaged from the simulation, which can be made arbitrarily long. This removes the problems one has if κ is estimated from runs with an initially nonuniform T-profile rapidly decaying toward a uniform T.

In practice the evaluation of κ requires the tabulation of T in radial zones, as well as the tabulation of the local and nonlocal energy fluxes in the radial direction. As for the bulk viscosity we must make sure that the linear trend assumed by Eq. (20) is indeed valid and that the proportionality factor is independent of A_ϵ in the limit of vanishing perturbation. Figure 8 provides an example of the κ evaluation, with $A_\epsilon = 0.2$. Altogether, the derived values of κ^{local} and $\kappa^{nonlocal}$ differed by less than about 5% between runs with $A_\epsilon = 0.01$–0.5. For still smaller amplitudes

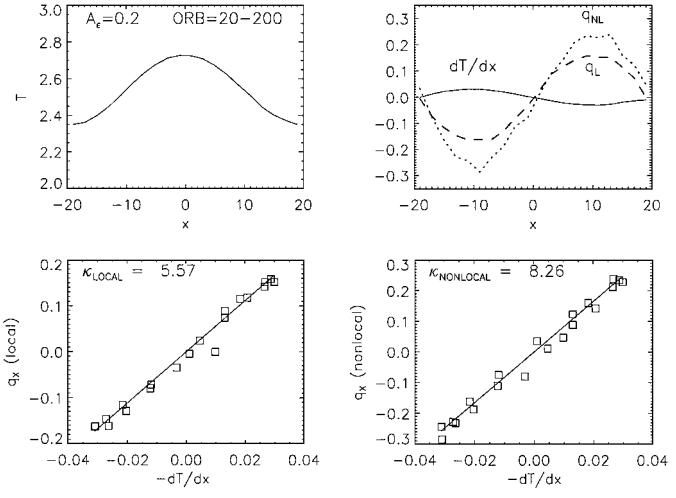

FIG. 8. Example of the determination of heat conductivity, for $\tau = 0.5$ and $\Omega_z/\Omega = 3.6$. The frame on the upper left shows the steady temperature profile (v_c is varied by 20% according to Eq. (23)). In the upper right the solid line represents the radial temperature gradient, while the dashed and dotted curves show the local and nonlocal heat fluxes, respectively. The lower frames show linear fits to values from all different zones, yielding the heat conduction coefficient. The units of temperature, heat flux, and kinematic heat conductivity are $(r\Omega)^2$, $(r\Omega)^3$, and $r^2\Omega$, respectively.

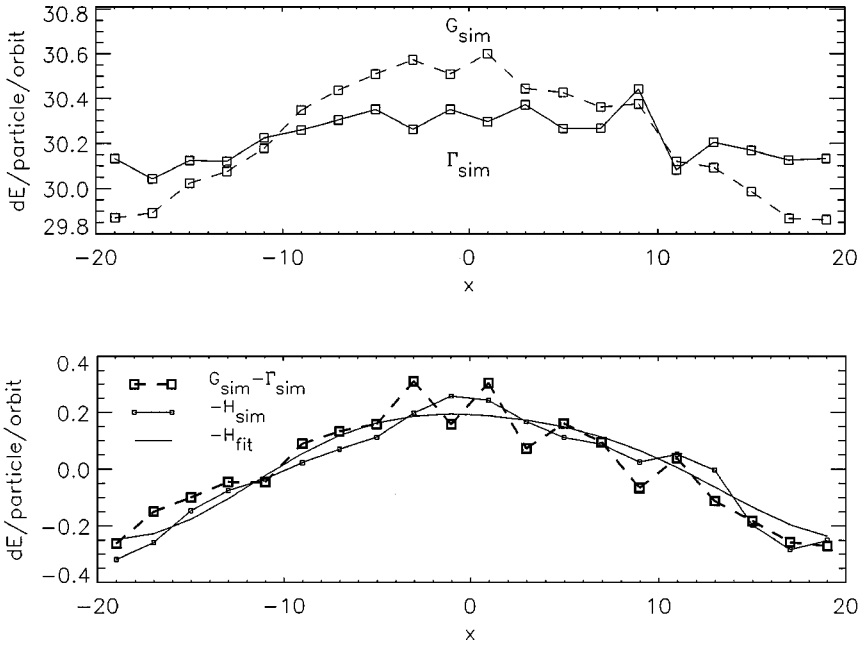

FIG. 9. Example of the energy balance in runs with steady nonuniform radial temperature profile. In the upper frame the viscous gain, $G_{sim} = \tau\nu[-\frac{3}{2}\Omega + \partial_x \delta u_y]^2$, and dissipation Γ_{sim} are shown. The lower frame shows the (negative of) heat conduction H_{sim}, calculated both directly from the measured energy flux ($H_{sim} = \partial_x(\tau q_{sim})$; thin line + open squares) and from the temperature gradient utilizing the fitted value of κ ($H^{fit}_{sim} = -\partial_x(\kappa\tau\partial_x T)$; solid thin lines). On the same frame $G_{sim} - \Gamma_{sim}$ (dashed line, large solid squares) is also shown. Note the difference in the scales between the upper and the lower frame: The near overlap of $G_{sim} - \Gamma_{sim}$ and $-H_{sim}$ indicates that the balance $G_{sim} - \Gamma_{sim} + H_{sim} = 0$ is very accurately satisfied. As in Fig. 6, change of energy/particle/orbital period is shown, normalized by $(r\Omega)^2$.

the values of $\kappa^{nonlocal}$ become strongly affected by noise. All the subsequent measurements were made with $A_\epsilon = 0.2$.

The derived values of κ can be verified by checking that the energy balance equation holds, not only for the system as a whole, but for each radial zone separately. Here we also take into account that due to the nonuniform temperature profile δu_x and δu_y do not necessarily vanish. In the presence of heat flow the energy balance reads

$$\frac{3}{2}\sigma(\partial_t + \mathbf{u}\cdot\boldsymbol{\nabla})T = -\hat{P} : \boldsymbol{\nabla}\mathbf{u} - \boldsymbol{\nabla}\cdot\mathbf{q} - \Gamma. \qquad (24)$$

It follows that for the pressure contribution we have

$$\hat{P} : \boldsymbol{\nabla}\mathbf{u} = p\,\partial_x\delta u_x - \left(\frac{4}{3}\eta + \xi\right)(\partial_x\delta u_x)^2 - \eta\left[-\frac{3}{2}\Omega + \partial_x\delta u_y\right]^2. \qquad (25)$$

For an x-dependent temperature profile this implies

$$\frac{3}{2}\sigma\,\delta u_x\,\partial_x T = -p\,\partial_x\delta u_x + \left(\frac{4}{3}\eta + \xi\right)(\partial_x\delta u_x)^2 + \eta\left[-\frac{3}{2}\Omega + \partial_x\delta u_y\right]^2 + \partial_x(\kappa_D\partial_x T) - \Gamma. \qquad (26)$$

In practice the δu_x terms turn out to be insignificant compared to δu_y, which in itself provides a small correction to the systematic shear. Dropping the terms containing δu_x, and using kinematic quantities, the energy equation implies

$$\tau\nu\left[-\frac{3}{2}\Omega + \partial_x\delta u_y\right]^2 + \partial_x(\tau\kappa\partial_x T) - \Gamma_{sim} = 0. \qquad (27)$$

Figure 9 provides an example of the magnitude of the viscous gain and dissipative loss terms, as well as the heat conduction. The case $\tau = 0.5$ is chosen, since then both local and nonlocal terms contribute significantly to the heat conduction. As can be seen the energy balance is fairly well satisfied in each zone.

3.3. Evaluation of Derivatives with Respect to Kinetic Temperature

The temperature derivatives of p, ν, and Γ_{sim} are evaluated by introducing a small uniform temperature deviation to the system. This is made by multiplying the shear corrected velocities of each particle, $\{\dot{x}, \dot{y} + 3/2\Omega x, \dot{z}\}$, by a constant factor f. This changes the temperature by a factor f^2 while maintaining the orientation of the velocity dispersion tensor. The various quantities of interest are then tabulated during short time intervals while the system returns to the steady state with $T = T_{st}$. The

derivatives are estimated with a linear fit between $\Delta T = T - T_{st}$ and the deviation of the collected quantities from their steady-state values. The same procedure can be repeated several times during each run to improve the statistics of the fit.

However, there are some difficulties in the method outlined above. Most importantly, the modification of particles' velocities introduces vertical oscillations to the system. In principle, this could be avoided by multiplying the z-coordinates of the particles with the same factor f. This however has the drawback that only $f > 1$ can be applied, since for $f < 1$ possible particle overlaps will invalidate the measurement. Also, altering the vertical profile can in itself modify the properties, so that the measurement might not correctly describe the partial derivative with respect to T alone. A possible solution would be to limit attention to just horizontal components of the velocity dispersion tensor, but this is not in accordance with the hydrodynamic approximation we are utilizing. Another way to reduce the influence of vertical oscillations is to perform several measurements with a different f and average over these runs that each possess slightly different oscillations. Figure 10 gives an example of such a measurement, for $\tau = 1$, $\Omega_z/\Omega = 3.6$. Altogether 11 runs are superposed, with $f = 0.5$–2.0. In the linear fit only a certain range of $|\Delta T|$ is used. The upper limit is chosen to make sure that derivatives correspond to the steady state, and the lower limit eliminates the noise around the steady state. Note that instead of the derivative of the cooling Γ_{sim}, we fit directly the quantity

$$E_T := \frac{2}{3\Omega}\partial_T\left(\Gamma_{sim} - \frac{9}{4}\Omega^2\tau\nu\right), \tag{28}$$

where the quantity in parenthesis measures the difference between the dissipational loss and viscous gain of energy. This quantity is chosen because this is the combination in which the cooling term enters the nonisothermal stability analysis (see Paper II).

In principle, we would also need to know the gradients of the above quantities with respect to surface density, for a fixed temperature. This is even more problematic to realize in simulations: Any change in the mean density, say by expanding the calculation region during the run, will also lead to rapid temperature adjustments. Therefore, we will approximate these derivatives by the differences of the above quantities between the steady-state values at various densities. This should be a fairly good approximation, especially since the steady-state temperature varies only weakly with density (see Fig. 11 in the next section).

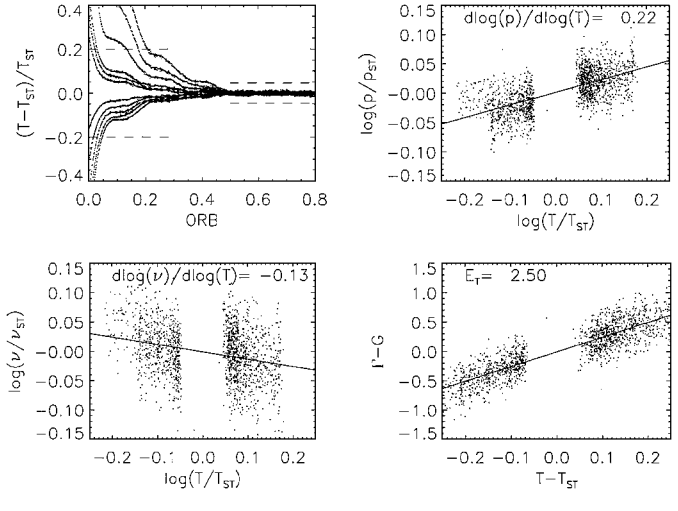

FIG. 10. Example of measuring the derivatives with respect to temperature, for $\tau = 1$ and $\Omega_z/\Omega = 3.6$. The frame on the upper left shows the decay of temperature perturbations to steady state: Each curve denotes a single simulation run and represent an average of 8 successive perturbations. Altogether 11 runs are shown, with velocity modification factor ranging between 0.5 and 2.0 (see the text for more explanations). The horizontal dashed lines indicate the temperature range used: In the current example only points where $0.05 < |T - T_{st}/T| < 0.2$ are used, where T_{st} indicates the steady-state temperature of the system. The three other frames show the fits to pressure, viscosity, and the difference between energy loss and gain, with respect to temperature.

4. RESULTS

We have carried out systematic measurements of the various steady-state quantities for τ up to 5 for three different values of the vertical frequency enhancement factor, $\Omega_z/\Omega = 1$, 2, and 3.6. In each case the particle radius is 1 m, the Saturnocentric distance is 100,000 km ($\Omega = 1.945 \times 10^{-4}$ s^{-1}), and the Bridges *et al.* impact model is assumed. The simulations utilize $N = 1000$ to 10,000 particles. Table I lists some of the parameters measured from simulations for selected values of τ.

Figure 11 (upper row) displays the dependence of the kinetic temperature T, pressure p, and shear viscosity ν on the optical depth. Both local and nonlocal contributions to p and ν are displayed. Pressure has been normalized by τ, so that the curves are more easily comparable; p^{local}/τ and ν^{local} are directly proportional to the trace and to the nondiagonal component of the velocity dispersion tensor, respectively. In accordance with previous simulations T first drops with τ but then starts to rise for larger τ. This decrease in T follows from the finite volume of particles, limiting the effective mean path between impacts and thus also the gain of energy from the systematic motion via local shear viscosity. In contrast, for a large enough τ nonlocal viscosity dominates the total viscosity and accounts for the rise of the steady-state temperature. The optical depth where the nonlocal viscosity component starts to exceed the local one depends on the vertical enhancement. For $\Omega_z/\Omega = 1$ and 3.6 this takes place at $\tau \approx 0.8$ and 0.3, respectively. Similarly, the nonlocal pressure exceeds the local one for $\tau \approx 1.0$ and 0.4. The energy dissipation Γ_{sim} as a function of τ was already shown in Fig. 6.

TABLE I
Various Quantities Measured from Simulations

τ	w_c/Ω	T	p	p^l/p^{nl}	ν	ζ	κ	$Dp/D\tau$	β	Dp/DT	$D\nu/DT$	E_T
						$\Omega/\Omega_z = 3.6$						
0.25	1.77	4.46	1.57	0.710	1.52	5.49	22.8	1.28	0.57	0.85	0.34	0.28
0.50	4.53	2.54	3.09	0.411	2.15	6.65	13.9	1.79	0.67	0.53	−0.04	0.72
1.00	14.8	1.73	10.8	0.160	3.87	8.27	16.1	2.19	1.15	0.21	−0.12	2.50
1.50	32.3	1.77	29.2	0.091	6.69	13.4	27.7	2.41	1.19	0.15	−0.10	3.79
2.00	55.8	1.91	59.4	0.064	9.52	20.2	38.9	2.72	1.55	0.18	0.08	4.50
						$\Omega/\Omega_z = 2.0$						
0.25	1.26	4.60	1.48	0.776	1.11	4.11	22.9	1.18	0.62	0.87	0.42	0.19
0.50	2.72	2.84	2.59	0.547	1.48	4.70	14.9	1.42	0.49	0.67	0.21	0.40
1.00	6.73	1.81	6.59	0.275	2.27	5.26	11.8	1.87	0.85	0.41	0.02	1.12
1.50	12.3	1.63	14.3	0.171	3.35	6.91	14.3	2.11	1.06	0.28	−0.12	2.23
2.00	19.8	1.63	26.9	0.121	4.63	9.24	18.1	2.26	1.16	0.28	−0.10	3.14
						$\Omega/\Omega_z = 1.0$						
0.25	0.71	5.03	1.45	0.867	0.66	2.93	17.5	1.11	0.80	0.92	0.57	0.08
0.50	1.44	3.85	2.62	0.733	1.03	3.93	19.9	1.22	0.57	0.82	0.39	0.18
1.00	3.07	2.48	4.98	0.498	1.42	4.15	13.6	1.45	0.51	0.66	0.17	0.57
1.50	5.01	1.96	8.47	0.346	1.82	4.28	11.5	1.67	0.70	0.51	0.13	0.81
2.00	7.30	1.74	13.6	0.257	2.27	4.84	11.7	1.85	0.88	0.39	−0.04	1.31

Note. Temperatures and pressures are scaled by $(r\Omega)^2$ and transport coefficients by $r^2\Omega$, as in the figures. D/DT and $D/D\tau$ denote logarithmic derivatives.

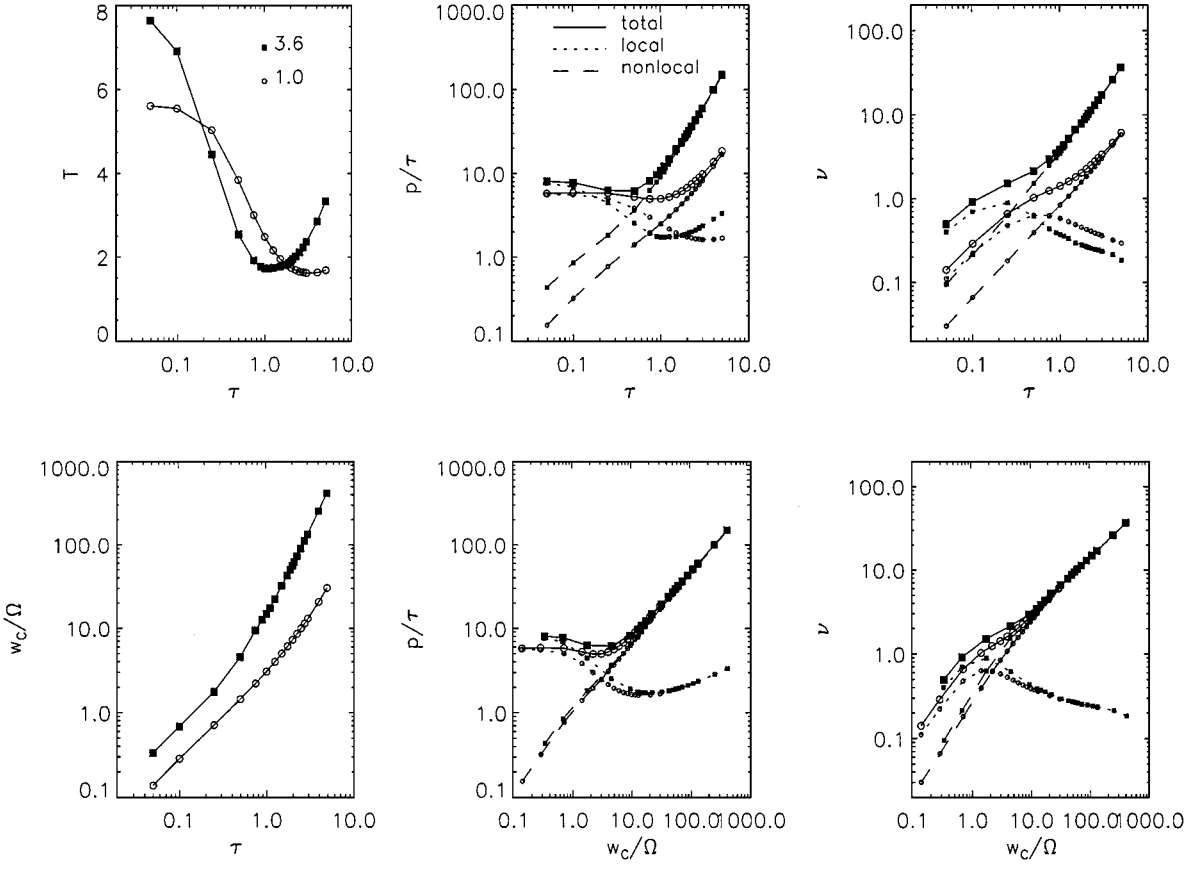

FIG. 11. The upper frames show the dependence of temperature, simulation pressure (divided by τ), and shear viscosity as a function of optical depth, for $\Omega_z/\Omega = 1.0$ and 3.6. In the lower left, the dependence of impact frequency on τ is shown, while the two remaining frames display p/τ and ν as a function of w_c.

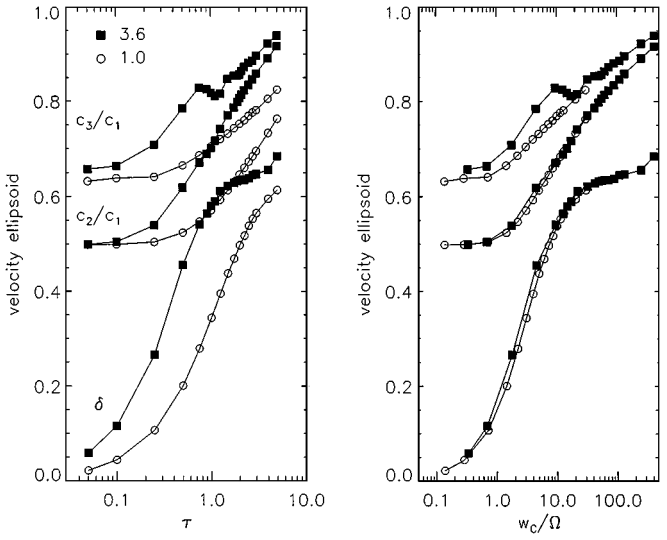

FIG. 12. Shape and orientation of the velocity dispersion tensor. The quantities c_1, c_2, and c_3 denote the principal axis values of the velocity dispersion tensor, while δ measures the deviation of the major principal axis from the radial direction (in radians). For small τ, c_1 and c_2 correspond to radial and tangential velocity dispersion, while c_3 measures the vertical dispersion for all values of τ.

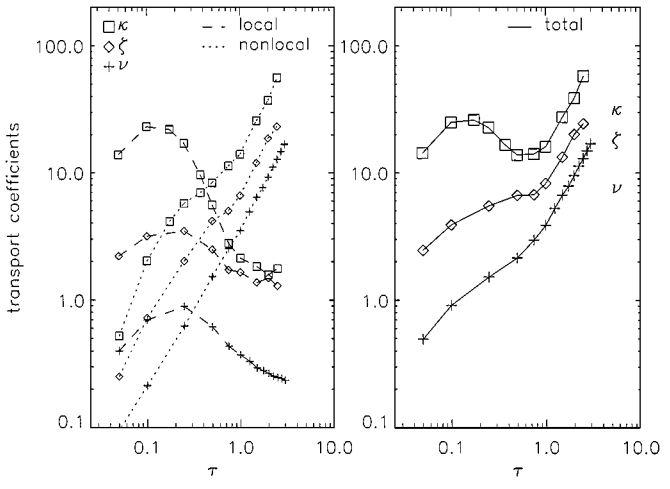

FIG. 13. Transport coefficients as a function of optical depth, for $\Omega_z/\Omega = 3.6$. In the left local and nonlocal contribution are shown separately, while in the right total values are displayed.

One of the main effects of the increased Ω_z/Ω is to enhance the impact frequency, so that the behavior of the system is similar to $\Omega_z = \Omega$ but with a higher τ. Indeed, when we look at p/τ and ν as functions of impact frequency w_c instead of τ (lower row of Fig. 11) it is clear that w_c is the actual quantity determining their behavior. In terms of impact frequency, the dominance of nonlocal terms begins when $w_c/\Omega \approx 2$–3, corresponding to roughly 15 impacts per orbital revolution.

The shape and orientation of the velocity dispersion tensor are shown in Fig. 12. The oscillations seen in the curves for $\Omega_z/\Omega = 3.6$, especially in the ratio c_3/c_1, are real, corresponding to the tendency of forming a layered vertical structure in the system, as found in Wisdom and Tremaine (1988). Again the velocity dispersion tensor depends mainly on w_c. Note that even for $\tau = 5$ the system is still fairly far from having an isotropic velocity dispersion tensor.

The different transport coefficients are compared in Fig. 13. For clarity only the case $\Omega_z/\Omega = 3.6$ is shown; the other two studied values lead to a same type of behavior (except for smaller values of coefficients; see Table I). For all values of τ we have total $\kappa > \zeta > \nu$, and the same order holds also separately for the local and nonlocal contributions. The local contribution to κ also peaks at smaller τ than that for ζ or ν. This again follows from the effect of reduced mean free path due to the finite volume of particles. Namely, κ is related to the energy flow, so it is dominated by the particles with the largest velocity deviations, and these are most prone to experience impacts. The nonlocal contribution to κ for small τ is relatively large, leading to a slanted S-shaped curve for the total κ, whereas both ζ and ν are monotonically increasing with τ. In general, the differences between local contributions are larger than those for the nonlocal ones. Because of this the ratios κ/ν and ζ/ν attain rather large values for small τ (Fig. 14). For large τ where nonlocal contributions dominate, the ratios seem to approach roughly constant values $\kappa/\nu \approx 4$ and $\zeta/\nu \approx 2$. The measurements are increasingly inaccurate for $\tau \to 0$, but it seems that the ratios at small τ are also limited, to $\kappa/\nu \approx 30$–40 and $\zeta/\nu \approx 6$–7. Again the behavior is dominated by the impact frequency, so that the ratios for different Ω_z/Ω are practically the same for a given w_c.

Figure 15 shows the logarithmic derivatives of viscosity and pressure with respect to τ. For small τ both p and ν are proportional to τ as the local contribution dominates. For intermediate τ, $\beta \equiv \partial \log(\nu)/\partial \log(\tau)$ decreases to about 0.5, near the maximum of ν^{local}, whereas for still larger τ the derivative rises above

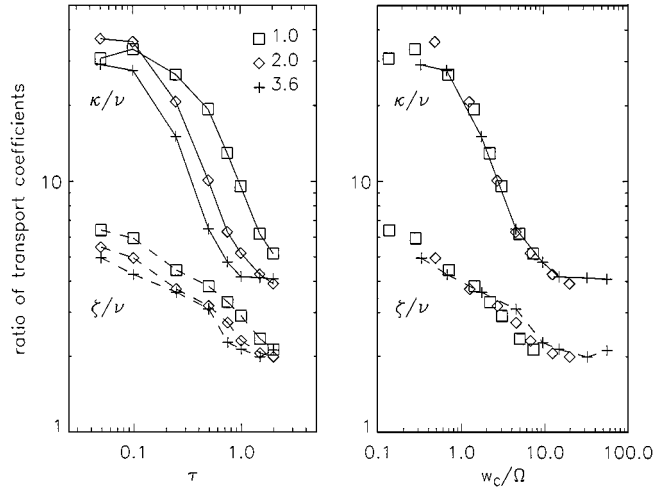

FIG. 14. Ratio of the transport coefficients (total values) for different values of Ω_z/Ω. In the right all measured ratios are shown together as a function of impact frequency.

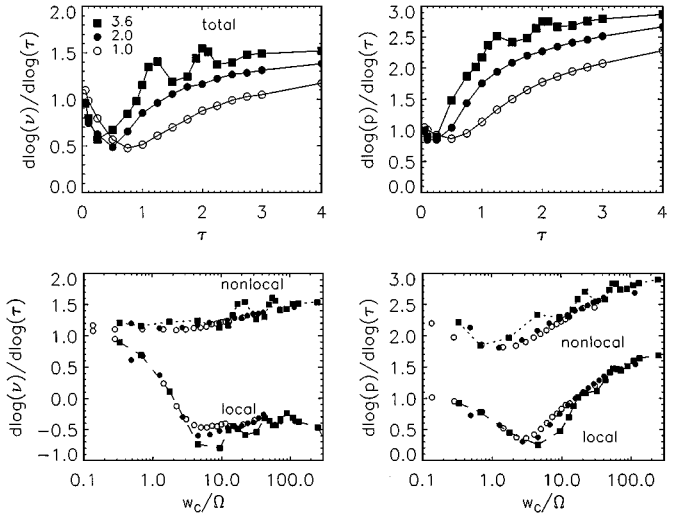

FIG. 15. Derivatives of shear viscosity and pressure with respect to density. In the upper frames the total values are shown as a function of τ for different values of Ω_z/Ω, while in the lower frames the local and nonlocal contributions are shown as a function of impact frequency.

unity, due to the nonlocal contribution. This rise is stronger for a larger Ω_z/Ω ratio, with β attaining unity at $\tau = 0.9,\ 1.3,$ and 2.5 for $\Omega_z/\Omega = 3.6,\ 2.0,$ and 1.0, respectively. This corresponds in each case to $w_c/\Omega \approx 10$, or about 60 impacts/orbital revolution. Again the curves for $\Omega_z/\Omega = 3.6$ show strong undulations, arising from the aforementioned tendency for a layered structure. For example, the z-distribution develops two density peaks between $\tau = 0.9$ and 1.04, three peaks between 1.5 and 1.75, and four between 2.25 and 2.5. The corresponding values of impact frequency are $w_c/\Omega \approx 15,\ 35,$ and 80, which in the lower frames are seen to be associated with the maxima and minima in the derivatives of local and nonlocal viscosities, respectively. The overall behavior of β for $1 < \tau < 2$ in the case $\Omega_z/\Omega = 3.6$ agrees well with $\beta = 1.26$ used in Schmit and Tscharnuter (1995). For the derivative of Γ_{sim} (not shown in the plot) we always find $\partial \log(\Gamma_{sim})/\partial \log(\tau) \approx \beta + 1$.

Figure 16 collects the measurements of temperature derivatives. Again the dependence on both τ and w_c is displayed to emphasize the dominant role of the latter quantity. At the limit of small τ both p and ν react roughly linearly to changes in T, as expected since they are dominated by local contributions. As τ increases, both $\partial \log(p)/\partial \log(T)$ and $\partial \log(\nu)/\partial \log(T)$

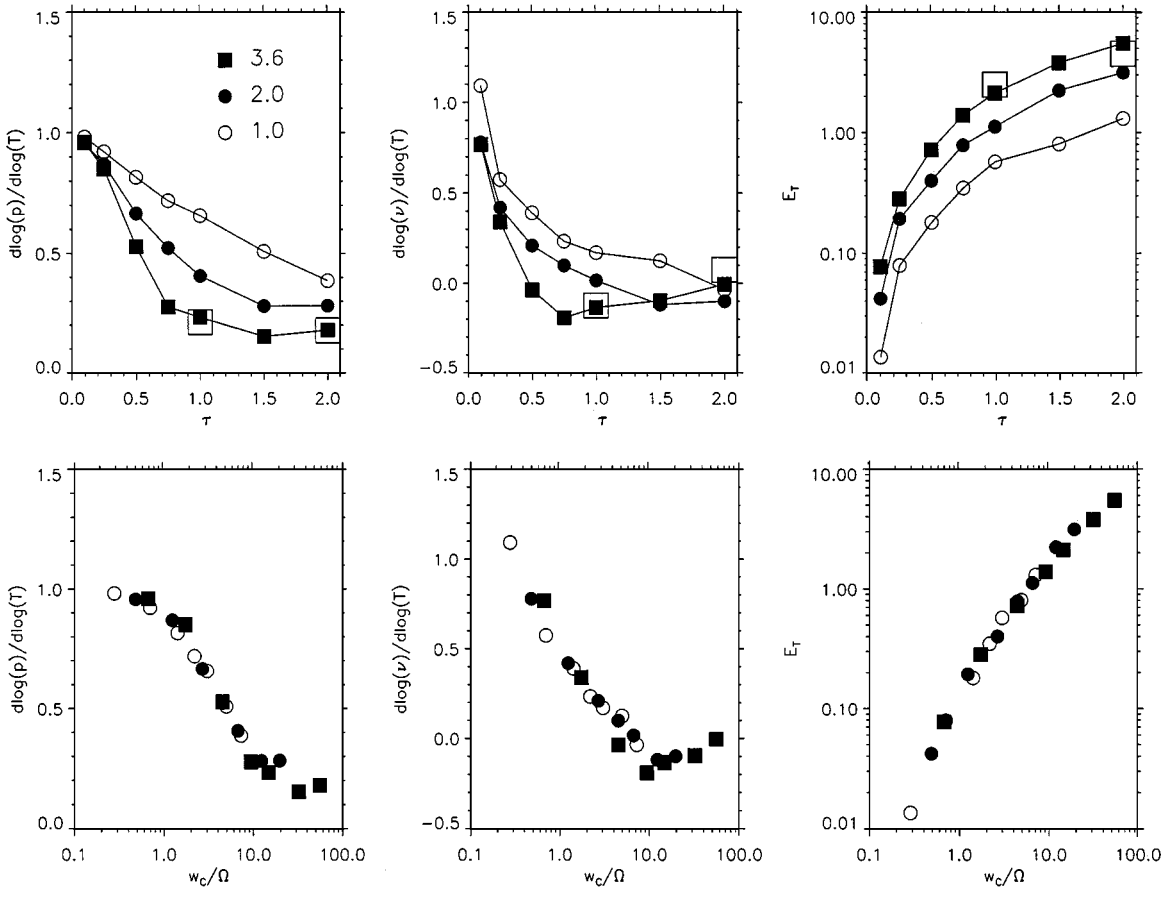

FIG. 16. Derivatives of pressure, shear viscosity, and net energy loss with respect to temperature. In the upper frames the derivatives are shown as a function of τ, separately for the three different values of Ω_z/Ω. In the lower frames the derivatives are shown as a function of impact frequency. Larger symbols indicate measurements where many individual runs were combined, as in Fig. 10.

decrease toward zero, with the latter achieving even slightly negative values for $w_c/\Omega \sim 10$. This indicates that for dense rings nonlocal pressure and viscosity are only weakly dependent on velocity dispersion, being rather dominated by the systematic velocity shear, manifesting the strongly non-Newtonian character of such granular flows. Note that the actual derivative $\partial p/\partial T = [\partial \log(p)/\partial \log(T)][p/T]$ increases monotonically with τ, since p increases strongly with τ while T varies only weakly. The quantity E_T rises almost linearly with w_c for $w_c/\Omega < 10$ but slows down somewhat for a larger impact frequency. The positive values of E_T indicate thermal stability as any temperature deviation will then tend to decay, with larger values indicating more rapid establishment of energy balance for a larger density. Altogether, the uncertainty of these derivatives is much larger than that of the steady-state quantities themselves.

In conclusion, the simulation measurements described above indicate that the main effect of enhanced vertical frequency comes through the increased impact frequency, thus shifting to smaller τ the behavior that would be seen in the nongravitating $\Omega_z/\Omega = 1$ case at larger densities. This holds for the steady-state quantities themselves and also for their derivatives with respect to temperature. Since the nonisothermal stability analysis predicts that the onset of overstability depends on the above quantities, most importantly on β, this means that also in the nongravitating case the overstability would be expected for a very large τ. In the case $\Omega_z/\Omega = 3.6$ our experiments with large simulation regions indicate that overstability sets in for $\tau \sim 0.85$, corresponding to $\beta \sim 0.93$. To check the behavior with $\Omega_z = \Omega$, three new large-scale experiments were carried out, with $\tau = 3, 4$, and 5, each extending for 500 orbital periods. In agreement with our previous, somewhat shorter runs, the first run with $\tau = 3$ is stable, although $\beta = 1.05$. The run with $\tau = 4$ ($\beta = 1.17$) shows some signs of marginal overstability (weak growth, limited to 150-m wavelength), but only the last run ($\beta = 1.25$) shows a clear overstability, although only the largest wavelength corresponding to $k = 1$, $\lambda = L_x = 310$ m grew in this run, with *e*-folding time of roughly 450 orbital periods. This suggests that $\beta_{cr} \sim 1$ is required for overstability for these parameter values (uni-sized particles of 1 m, Bridges *et al.*'s coefficient of restitution); the small difference between the cases reflects the slight difference in other parameters. In Paper II we show more detailed comparisons between predicted and measured growth times.

All the experiments so far have referred to the elasticity model of Bridges *et al.* To briefly check whether the derived transport coefficients have more general validity a few experiments with different scale parameter v_c in Eq. (2) were carried out. We chose $v_c/v_B = 5$, for which case the steady-state velocity dispersion is roughly doubled as compared to $v_c/v_B = 1$, and carried out measurements of ν, ζ, and κ for $\tau = 1$ (see Table II). The ratios κ/ν and ζ/ν seem to be fairly little affected by this change in the elasticity model. The values of β are also shown in Table I and indicate that in the case $v_c/v_B = 5$ the system with $\Omega_z/\Omega = 3.6$ now falls marginally outside the parameter region of overstability estimated above ($\beta \approx 0.9$). Indeed, in a corresponding large-scale run no overstability was obtained. However, when τ is increased to 1.5, the $v_c/v_B = 5$ case leads to overstability ($\beta \approx 1.1$) as well.

TABLE II
Transport Coefficients for τ = 1 for Two Different Scale Parameters in Bridges *et al.*'s formula

Ω_z/Ω	v_c/v_B	$\sqrt{T}$	ν	ζ	κ	κ/ν	ζ/ν	β
1.0	1	1.57	1.42	4.2	13.6	9.6	2.9	0.51
1.0	5	3.07	3.06	7.7	29.9	9.8	2.5	−0.20
3.6	1	1.31	3.87	8.3	16.1	4.2	2.1	1.15
3.6	5	2.08	4.68	11.0	19.8	4.2	2.3	0.89

Note. Velocity dispersion $\sqrt{T}$ is scaled by $r\Omega$ and transport coefficients by $r^2\Omega$, as in the figures.

It is also of interest to estimate the critical β for overstability in self-gravitating runs. For the case studied in Fig. 5 ($\rho = 225$ kg m^{-3}, τ varied) the onset of overstability takes place in the range $\tau = 1.0$–1.2. If the viscosities are evaluated in the same manner as for the runs with enhanced Ω_z/Ω, this corresponds again to $\beta = 1.0$–1.1. However, this is only approximative, as it neglects the gravitational viscosity, corresponding to momentum flow due to the gravitational scattering by the wakes (Daisaka *et al.* 2000). Nevertheless, wakes are fairly weak in this case.

Finally, we also made runs with the three different ring models studied in detail in Mosqueira (1996), corresponding to the Uranian δ and ϵ rings and Saturn's B ring ($\tau = 0.62$, 1.04, and 1.8, respectively). Since the calculation region has a fixed radial size these runs correspond to the $q = 0$ experiments in Mosqueira (1996), i.e., no streamline distortion. In these experiments the enhancement factor for vertical frequency was calculated from the instantaneous vertical thickness of the system, in the same manner as in Mosqueira (1996),

$$\Omega_z^2 = \Omega^2 + \frac{8\pi G\,\tau r\rho}{3H_{\rm eff}}, \tag{29}$$

where $H_{\rm eff} = \sqrt{\langle z^2\rangle} + r$, with r denoting the particle radius. Also, the appropriate values of Ω were used. The mean enhancement factors obtained in this manner were $\Omega_z/\Omega = 1.59,\ 2.04$, and 3.14 for these three models. In agreement with the perturbed runs carried out in Mosqueira (1996), the first two models were stable also in the unperturbed case (no growth of oscillations during 150 orbital periods), whereas in the third model a clear axisymmetric overstability was seen: in a run with total radial extent of 620 m the fastest growing mode with $k = 5,\ \lambda = 124$ m had a ten-fold time of about 20 orbital periods.

5. SUMMARY AND DISCUSSION

Our self-gravitating simulations provide a first direct demonstration of viscous overstability in a dense unperturbed collisional ring. For parameters resembling those typically inferred for dense parts of Saturn's B ring this instability manifests as systematic axisymmetric density, velocity, and temperature oscillations, with radial scales ~100 m and oscillation periods

close to the orbital period. Several tests ensured that the results are not affected by the periodic boundary conditions employed in the simulations, thus supporting the hypothesis that similar free axisymmetric oscillations could spontaneously grow in real ring systems. The requirement for the onset of overstability is that the rings have a high filling factor, which is the case for a Bridges *et al.* (1984) elasticity model for meter-sized particles in self-gravitating rings with $\tau > 1$.

A hydrodynamical treatment of dense unperturbed rings (Schmit and Tscharnuter 1995) has predicted overstable behavior. However, the conditions we find for overstability are clearly more stringent than predicted by their hydrodynamic treatment, as indicated by the stability of simulated non-self-gravitating rings for $\tau \sim 1$. Oscillatory instability was theoretically suggested also by Borderies *et al.* (1985) for forced density waves in dense rings, under conditions which were subsequently explored by simulations of Mosqueira (1996). Specifically, Mosqueira (1996) found that the condition for density wave overstability was fulfilled in his B-ring model with $\tau = 1.8$, but not for his ϵ-ring model with $\tau = 1.04$, in qualitative agreement with our results for unperturbed free oscillations. Still, based on these two examples it is not yet completely clear weather these two cases have similar stability boundaries.

Our experiments with particle–particle self-gravity indicate that axisymmetric overstability can coexist with nonaxisymmetric Julian–Toomre wakes forming in dense self-gravitating rings. However, the presence of *strong* wakes seems to suppress overstable oscillations, as seen by comparing runs with fixed surface density but with different internal density of particles. When we are near the stability boundary, any small reduction in the amplitude of wakes can promote overstable oscillations. For example, when the calculations of Fig. 1 for $\rho = 450$ kg m^{-3} are repeated by limiting the region from which the self-gravity is calculated to one λ_{cr}, axisymmetric oscillations become clearly visible in the direct plots for $\tau \sim 1$. The same is also true when using smaller rectangular calculation regions (size $< 2\lambda_{cr}$). However, in such a small-scale simulation it may be difficult to recognize the axisymmetric overstability, as complete unstable wavelengths do not fit into the calculation region. Indeed, it is very likely that the coherent velocity oscillation reported recently by Daisaka and Ida (1999), seen in their local simulations, manifests such incompletely covered viscous overstability, rather than being caused by any gravitational scattering by wakes. Unluckily, our current computational resources do not allow extended simulations with larger ρ's for τ's exceeding unity (this follows from the $\rho^2\tau^3$ dependence of the required number of particles) (Salo 1995). For example, to study particles with solid ice density, $\rho = 900$ kg m^{-3}, with $\tau = 2$ would require $N \sim 10^6$ even if limiting the study to identical particles.

The presence of gravitational wakes complicates any analytical study of overstability, as the system cannot be described by a spatially uniform ground state. However, we have shown that a qualitatively similar viscous overstability can be obtained when particle–particle self-gravity is approximated by an enhanced frequency of vertical oscillations, $\Omega_z/\Omega > 1$. As shown by previous simulations (Wisdom and Tremaine 1988) this approximation leads to strongly enhanced impact frequency and a steeper dependence of viscosity on density. Indeed, with the value $\Omega_z/\Omega = 3.6$, chosen in Wisdom and Tremaine (1988) to represent the dense B ring, this method also leads to overstability in the regime $\tau \sim 1$. Besides being computationally much faster than the inclusion of particle–particle self-gravity, this treatment has the important advantage that it leads to a uniform ground state, from which the growth of overstable oscillations can be analyzed.

We have employed local simulations also for the direct evaluation of transport coefficients for simulations with $\Omega_z/\Omega =$ 1.0–3.6. A large number of individual runs were performed, with calculation regions small enough to prevent the growth of overstable modes. For shear viscosity the method devised by Wisdom and Tremaine (1988) was used. Shear viscosity is related to the radial flow of tangential momentum in the presence of the systematic velocity shear. The local component of viscosity was obtained from the flow of momentum accompanying the epicyclic random motions of particles and is related to the nondiagonal component of the velocity dispersion tensor. For steady-state systems this could be measured with good accuracy by averaging the whole ensemble of simulation particles, and also over time, a fact first utilized extensively by Wisdom and Tremaine (1988). However, in the case where typical particle excursions between impacts are not large compared to their sizes, there is another important, so-called nonlocal component Araki and Tremaine 1986, Shukman 1984), related to the flow of tangential momentum in impacts between particles whose centers are at slightly different radial distances (hence the term "nonlocal"). The nonlocal flow can also be directly measured in simulations by time averaging over collisional momentum changes in impacts. In fact, this nonlocal component dominates in systems with high optical depth and large filling factor and leads to the strongly nonlinear behavior of viscosity as a function of τ. The measurement of nonlocal viscosity also followed the method of Wisdom and Tremaine (1988).

For the evaluation of heat conductivity a somewhat different procedure was employed, since in the steady state there is no temperature gradient in the local system (however, the tangential velocity shear is always present). In principle, we could introduce an initial gradient of temperature and observe the heat flux connected to it. However, this poses problems as the temperature gradient itself and the other properties of the system are then continuously changing. A more reliable way to measure heat conductivity is to make the amount of dissipation (via elasticity) depend on the radial position. A slightly different collisional steady state then follows in various parts of the system, accompanied by a steady temperature gradient and heat flux. Provided that the elasticity is only slightly different at different positions, this will provide an estimate of heat conductivity characteristic to the mean value of dissipation in the system. As in the case of viscosity, heat conductivity also contains a nonlocal contribution.

Bulk (or expansion) viscosity has not been previously measured in connection to planetary rings. This quantity is related to what happens in the compression of the system. If the work delivered to the system when it is compressed is not balanced by the work relieved in the expansion phase, this extra dissipation is attributed to bulk viscosity. The measurement of bulk viscosity from simulations was made directly from its definition. We introduced a sinusoidal standing radial velocity perturbation to the system and observed the proportionality between compression and the deviation of the instantaneous pressure from its equilibrium value. Again, both local and nonlocal components, associated with local and nonlocal pressure, were significant. Note that bulk viscosity could also be measured by the simulational method of Mosqueira (1996), where the azimuth-dependent radial width of the local simulation region induces compression. In principle this could provide an even more accurate measurement, as averages over arbitrarily long collection periods could be used.

Besides the transport coefficients, the nonisothermal stability analysis also requires knowledge of how the dissipation, pressure, and shear viscosity depend on temperature for a fixed density. These were also measured directly from local simulations, with methods similar to those used for the evaluation of transport coefficients. The derivatives with respect to density were estimated from the differences between steady-state values for different densities, justified by the weak dependence of temperature on density.

Our measurements indicated that both κ and ζ generally exceed ν, with the asymptotic values at large τ being $\kappa/\nu \approx 4$ and $\zeta/\nu \approx 2$. Strictly speaking this is valid only for the parameter combination we have adopted: meter-sized identical particles with Bridges *et al.*'s elasticity model. However, a few examples with somewhat thicker systems gave similar ratios, although the absolute values of transport coefficients were larger. Interestingly, the above asymptotic ratios for transport quantities are qualitatively similar to those derived from the Enskog kinetic theory of dense systems, which gives $\kappa/\nu \approx 4$ and $\zeta/\nu \approx 1.3$ (Chapman and Cowling 1970), while if allowance for a small amount of dissipation is made (Jenkins and Richman 1985), κ/ν decreases while ζ/ν increases slightly (Fig. 17). Typically, nonlocal contribution to both pressure and viscosity exceed local ones at large τ's, corresponding to impact frequency $w_c/\Omega >$

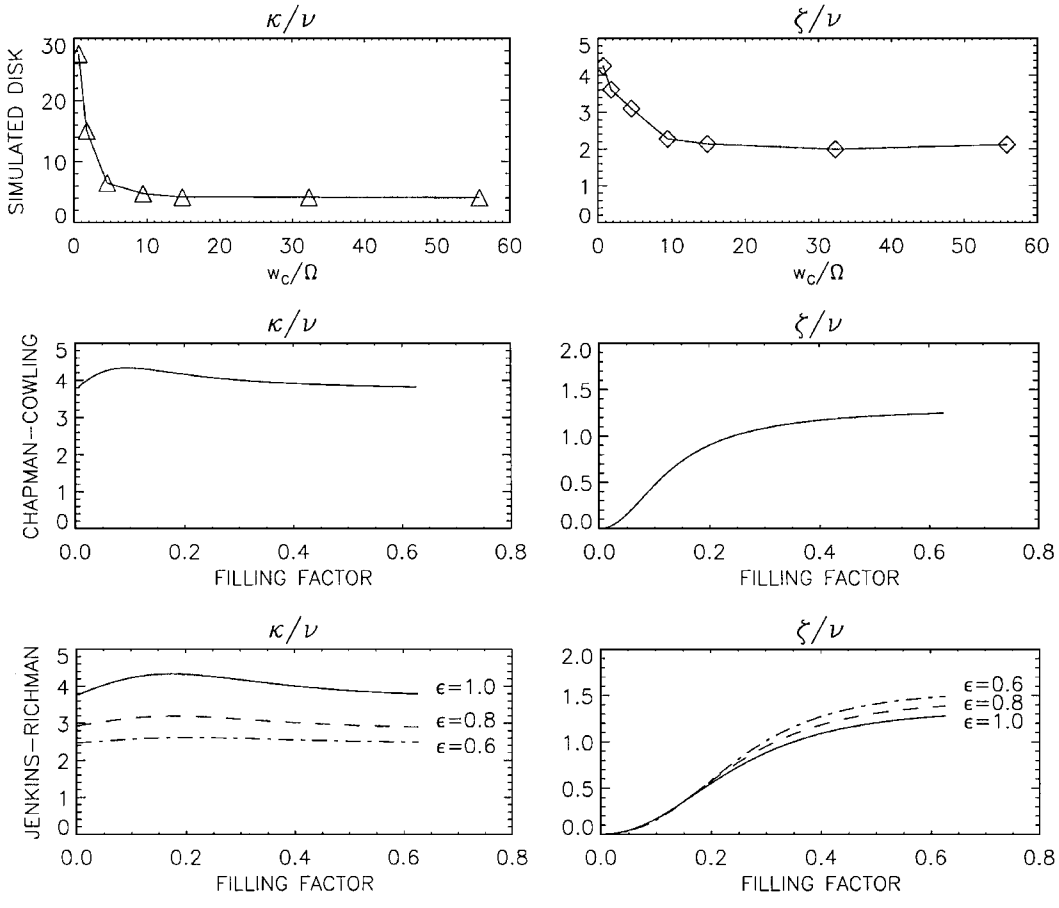

FIG. 17. Comparison of the ratio of transport quantities obtained in simulations (upper row) with those calculated for dense hard-sphere gases by Chapman and Cowling (1970) (middle row) and by Jenkins and Richman (1985) for dissipative particles (lowermost row). In simulations asymptotic values are obtained when $w_c/\Omega > 10$, corresponding to mean volume filling factor within $|z| < H/2$ exceeding about 0.4.

2–3. In general, w_c was found to be the dominant factor determining all quantities, especially in the limit where nonlocal contributions were large.

The main factor determining the onset of axisymmetric overstability is the dependence of viscosity on density. In the current simulations we found $\beta_{cr} \sim 1$ as a rough condition for the onset of overstability. For $\Omega_z/\Omega = 3.6$ this is achieved for $\tau \sim 1$, as in our self-gravitating runs, whereas for $\Omega_z/\Omega = 1$ the overstable regime is shifted to $\tau \sim 4$, explaining the lack of overstability in our previous nongravitating simulations. The $\beta_{cr} \sim 1$ limit is clearly larger than the $\beta_{cr} \sim 0$ suggested by the isothermal linear stability analysis in Schmit and Tscharnuter (1995). However, the increased stability is in accordance with the nonisothermal analysis in Spahn *et al.* (2000). In part the stability seems to be due to the temperature oscillations accompanying the density and velocity oscillations, and in part it is due to bulk viscosity exceeding shear viscosity. A detailed comparison between simulations and hydrodynamical analysis is presented in a separate paper (Paper II).

ACKNOWLEDGMENTS

We are grateful to Dr. Ignacio Mosqueira and Dr. Keiji Ohtsuki for their very useful comments and suggestions. This work was supported by the Academy of Finland and by the Deutsche Forschungsgemeinschaft, Grant Sp 384/7-3.

REFERENCES

Araki, S. 1991. The dynamics of particle disks III. Dense and spinning particle disks. *Icarus* **90**, 139–171.

Araki, S., and S. Tremaine 1986. The dynamics of dense particle disks. *Icarus* **65**, 83–109.

Blumenthal, G. R., L. T. Yang, and D. N. C. Lin 1984. On the overstability of axisymmetric oscillations in thin accretion disks. *Astrophys. J.* **287**, 774–784.

Borderies, N., P. Goldreich, and S. Tremaine 1985. A granular flow model for dense planetary rings. *Icarus* **63**, 406–420.

Borderies, N., P. Goldreich, and S. Tremaine 1986. Nonlinear density waves in planetary rings. *Icarus* **68**, 522–533.

Bridges, F., A. Hatzes, and D. N. C. Lin 1984. Structure, stability and evolution of Saturn's rings. *Nature* **309**, 333–335.

Brilliantov, N., F. Spahn, J.-M. Hertzsch, and T. Pöschel 1996. Model for collisions in granular gases. *Phys. Rev. E* **53**, 5382–5392.

Chapman, S., and T. Cowling 1970. *The Mathematical Theory of Non-uniform Gases.* Cambridge University Press, Cambridge, UK.

Cuzzi, J. N., J. J. Lissauer, and F. H. Shu 1981. Density waves in Saturn's rings. *Nature* **292**, 703–707.

Cuzzi, J. N., J. J. Lissauer, L. Esposito, J. Holberg, E. Marouf, G. Tyler, and A. Boischot 1984. Saturn's rings: Properties and processes. In *Planetary Rings* (R. Greenberg and A. Brahic, Eds.), pp. 73–199. Univ. of Arizona Press, Tucson.

Daisaka, H., and S. Ida 1999. Spatial structure and coherent motion in dense planetary rings induced by self-gravitational instability. *Earth Planets Space* **51**, 1195–1213.

Daisaka, H., H. Tanaka, and S. Ida 2000. Structure and transport process in dense planetary ring. *Bull. Am. Astron. Soc.* **32**, 4907.

Durisen, R. H. 1995. An instability in planetary rings due to ballistic transport. *Icarus* **115**, 66–85.

Esposito, L. W., M. Ocallaghan, K. E. Simmons, C. W. Hord, R. A. West, A. L. Lane, R. B. Pomphrey, D. L. Coffeen, and M. Sato 1983. Voyager photopolarimeter stellar occultation of Saturn's rings. *J. Geophys. Res.* **88**, 8643–8649.

Goldreich, P., and S. Tremaine 1978. The formation of the Cassini division in Saturn's rings. *Icarus* **34**, 240–253.

Goldreich, P., and S. Tremaine 1982. The dynamics of planetary rings. *Annu. Rev. Astron. Astrophys.* **20**, 249–283.

Goldreich, P., N. Rappaport, and B. Sicardy 1995. Single sided shepherding. *Icarus* **118**, 414–417.

Goertz, C. K., and G. Morfill 1988. A new instability of Saturn's ring. *Icarus* **74**, 325–330.

Hämeen-Anttila, K. A. 1978. An improved and generalized theory for the collisional evolution of Keplerian orbits. *Astrophys. Space Sci.* **58**, 477–519.

Hänninen, J., and H. Salo 1995. Formation of isolated narrow ringlets by a single satellite. *Icarus* **117**, 435–438.

Hertzsch, J.-M., H. Scholl, F. Spahn, and I. Katzorke 1997. Simulations of collisions in planetary rings. *Astron. Astrophys.* **320**, 319–324.

Horn, L. J., and J. N. Cuzzi 1996. Characteristic wavelengths of irregular structure in Saturn's B ring. *Icarus* **119**, 285–310.

Jenkins, J. T., and M. T. Richman 1985. Grad's 13-moment system for a dense gas of inelastic spheres. *Arch. Ration. Mech. Anal.* **87**, 355–377.

Julian, W. H., and A. Toomre 1966. Non-axisymmetric responses of differentially rotating disks of stars. *Astrophys. J.* **146**, 810–830.

Kato, S. 1978. Pulsational instability of accretion disks to axially symmetric oscillations. *Mon. Not. R. Astron. Soc.* **185**, 629–642.

Lane, A. L., C. W. Hord, R. A. West, L. W. Esposito, D. L. Coffeen, M. Sato, K. E. Simmons, R. B. Pomphrey, and R. B. Morris 1982. Photopolarimetry from Voyager 2—Preliminary results on Saturn, Titan, and the rings. *Science* **215**, 537–543.

Lewis, M. C., and G. R. Stewart 2000. Collisional dynamics of perturbed planetary rings. I. *Astron. J.* **120**, 3295–3310.

Lin, D. N. C., and P. Bodenheimer 1981. On the stability of Saturn's rings. *Astrophys. J.* **248**, L83–86.

Lissauer, J. J., F. H. Shu, and J. N. Cuzzi 1981. Moonlets in Saturn's rings. *Nature* **292**, 707–711.

Longaretti, P.-Y., and N. Rappaport 1995. Viscous overstabilities in dense narrow planetary rings. *Icarus* **116**, 376–396.

Lukkari, J. 1981. Collisional amplification of density fluctuations in Saturn's rings. *Nature* **292**, 433–435.

Lukkari, J., and H. Salo 1984. Numerical simulations of collisions in self-gravitating systems. *Earth, Moon, Planets* **31**, 1–13.

Mosqueira, I. 1996. Local simulations of perturbed dense planetary rings. *Icarus* **122**, 128–152.

Ohtsuki, K. 1999. Evolution of particle velocity dispersion in a circumplanetary disk due to inelastic collisions and gravitational interactions. *Icarus* **137**, 152–177.

Ohtsuki, K., and H. Emori 2000. Local N-body simulations for the distribution and evolution of particle velocities in planetary rings. *Astron. J.* **119**, 403–416.

Papaloizou, J. C. B., and D. N. C. Lin 1988. On the pulsational overstability in narrowly confined viscous rings. *Astrophys. J.* **331**, 838–860.

Press, W. H., S. A. Teukolsky, W. T. Vetterling, and B. P. Flannery 1992. *Numerical Recipes in FORTRAN.* Cambridge Univ. Press, Cambridge, UK.

Rosen, P. A., G. L. Tyler, E. A. Marouf, and J. J. Lissauer 1991. Resonance structures in Saturn's rings probed by radio occultation. II—Results and interpretation. *Icarus* **93**, 25–44.

Salo, H. 1991. Numerical simulations of dense collisional systems. *Icarus* **90**, 254–270. See also Erratum, *Icarus* **92**, 367–368.

Salo, H. 1992a. Gravitational wakes in Saturn's rings. *Nature* **359**, 619–621.

Salo, H. 1992b. Numerical simulations of dense collisional systems: II. Extended distribution of particle sizes. *Icarus* **96**, 85–106.

Salo, H. 1995. Simulations of dense planetary rings: III. Self-gravitating identical particles. *Icarus* **117**, 287–312.

Salo, H. 2001. Numerical simulations of collisional dynamics of planetary rings. In *Granular Gases* (T. Pöschel and S. Luding, Eds.), Lecture Notes in Physics Vol. 564, pp. 330–349. Springer-Verlag, Berlin.

Schmidt, J., F. Spahn, O. Petzschmann, and H. Salo 1999. Vertical distribution of temperature and density in a planetary ring. *Astron. Astrophys.* **345**, 646–652.

Schmidt, J., H. Salo, F. Spahn, and O. Petzschmann 2001. Viscous overstability in Saturn's B ring: II. Hydrodynamic theory and comparison to simulations *Icarus* **153**, 316–331.

Schmit, U., and W. Tscharnuter 1995. A fluid dynamical treatment of the common action of self-gravitation, collisions, and rotation in Saturn's B-ring. *Icarus* **115**, 304–319. [ST]

Schmit, U., and W. Tscharnuter 1999. On the formation of the fine–scale structure in Saturn's B ring. *Icarus* **138**, 173–187.

Shu, F. H., L. Dones, J. J. Lissauer, C. Yuan, and J. N. Cuzzi 1985. Nonlinear spiral density waves—Viscous damping. *Astrophys. J.* **299**, 542–573.

Shukman, I. G. 1984. Collisional dynamics of particles in Saturn's rings. *Sov. Astron.* **28**, 574–584.

Smith, B. A., and 28 colleagues 1982. A new look at the Saturn system—The Voyager 2 images. *Science* **215**, 505–537.

Spahn, F., and H. Sponholz 1989. Existence of moonlets in Saturn's rings inferred from the optical depth profile. *Nature* **339**, 607–608.

Spahn, F., J.-M. Hertzsch, and N. Brilliantov 1995. The role of particle collisions for the dynamics in planetary rings. *Chaos, Solitons, Fractals* **5**, 1945–1964.

Spahn, F., J. Schmidt, O. Petzschmann, and H. Salo, 2000. Stability analyses of a Keplerian disk of granular grains: influence of the thermal diffusion. *Icarus* **145**, 657–660.

Stewart, G. R., D. N. C. Lin, and P. Bodenheimer 1984. Collision induced transport properties in planetary rings. In *Planetary Rings* (R. Greenberg and A. Brahic, Eds.), pp. 447–512. Univ. of Arizona Press, Tucson.

Toomre, A. 1964. On the gravitational stability of a disk of stars. *Astrophys. J.* **139**, 1217–1238.

Toomre, A., and A. J. Kalnajs 1991. Spiral chaos in an orbital patch. In *Dynamics of Disc Galaxies* (B. Sundelius, Ed.), pp. 341–358. Göteborgs University and Chalmers University of Technology, Göteborg, Sweden.

Ward, W. R. 1981. On the radial structure of Saturn's rings. *Geophys. Res. Lett.* **8**, 641–643.

Wisdom, J., and S. Tremaine 1988. Local simulations of planetary rings. *Astron. J.* **95**, 925–940.